Journal of Intelligent & Robotic Systems (2020) 99:837–857
https://doi.org/10.1007/s10846-020-01154-8

Hydrodynamic Parameter Estimation for an Anguilliform-inspired Robot

Aditi Raj[1] · **Atul Thakur**[2]

Received: 5 June 2019 / Accepted: 13 January 2020 / Published online: 26 February 2020

Abstract

This paper presents an optimization-based approach to estimate the hydrodynamic parameters namely drag and added mass coefficients from free-running experiments conducted on an in-house developed Anguilliform-inspired robot. The objective of the optimization problem is to estimate the hydrodynamic parameters that minimize the differences between the trajectories obtained from the simulations and the physical experiments when operated for identical gait parameters and controller gains for both the straight and the turning motions. The hydrodynamic parameters obtained from the developed approach leads to a maximum root-mean-square (RMS) position error of 0.183 BL and a maximum RMS velocity error of 0.03 BL/s between the trajectories obtained from simulations and experiments. Experimental results suggest that the parameters estimated using the developed approach can be useful in predicting the robot's motion accurately. Accurate robot motion prediction is the fundamental requirement for localization, collision prediction, and motion planning algorithms which in turn are required for automated inspection, maintenance, and repair of sub-sea structures using Anguilliform-inspired robots.

Keywords Parameter estimation · Fish-inspired robotics · Underwater robotics · Optimization · Anguilliform-inspired robot

1 Introduction

Anguilliform-inspired robots, due to their slender and hyper-redundant bodies, can allow automated inspection, maintenance, and repair of sub-sea structures which involve exploration of narrow regions [1]. In the aforementioned applications, the capability of dynamics model based motion prediction is often used for collision prediction [2–4] and motion planning [5–8]. The dynamics of Anguilliform-inspired robots is complicated due to their hyper-redundant structure and interaction with the fluid environment. Although, dynamics-based motion models for Anguilliform-inspired robots have been reported in the past [9–13], the hydrodynamic parameters namely, drag and added mass coefficients used in such models are often estimated using approximate analytical formulae [14, 15] based on slender body assumptions owing to which the fidelity of the motion prediction is not satisfactory resulting in a large difference between the trajectories obtained by simulations employing hydrodynamic parameters obtained via analytical formulae with respect to the physical experiments. Hence, the literature suggests that the estimation of hydrodynamic parameters using physical experiments can yield better results as compared to the analytical formulae based hydrodynamic parameters [9]. Most of the research in the field of hydrodynamic parameter estimation has been done for unmanned surface vehicles (USVs) and autonomous underwater vehicles (AUVs) that, to a great extent, have rigid structure and hence cannot be applied to hyper-redundant underwater robots having non-rigid structure.

The only research reported in the area of hydrodynamic parameter estimation of Anguilliform-inspired robots is

Electronic supplementary material The online version of this article (https://doi.org/10.1007/s10846-020-01154-8) contains supplementary material, which is available to authorized users.

✉ Aditi Raj
aditiraj.pme13@iitp.ac.in

Atul Thakur
athakur@iitp.ac.in

[1] Department of Mechanical Engineering, Mechatronics Instrumentation and Control Laboratory, Indian Institute of Technology Patna, Bihta, Bihar, 801106, India

[2] Department of Mechanical Engineering, Indian Institute of Technology Patna, Bihta, Bihar, 801106, India

by Kelasidi et al., [1]. They used a curve fitting based approach on experimental data to estimate the hydrodynamic parameters. A comparison of average speeds obtained from the simulations and the physical experiments was performed and a maximum error of 12.92% was reported. However, the reported validation experiments presented by Kelasidi et al., 2016 were performed for the robot performing simple straight-line following motion. An approach for determining hydrodynamic parameters for underwater hyper-redundant Anguilliform-inspired robots and a detailed validation of the determined parameters for complex trajectories involving multiple waypoints has, thus, not been reported before. This paper reports an optimization-based approach for the estimation of hydrodynamic parameters for a wider range of gait parameters applicable for straight-line as well as turning motions.

This paper also reports the errors in terms of the difference between the trajectories obtained from the physical experiments and the simulations using the estimated hydrodynamic parameters; it is a more informative measure of the robot motion compared to the average speed. It is envisaged that the developed approach can be used for motion prediction that can be further used in localization, collision prediction, and motion planning in automated inspection, maintenance, and repair of sub-sea structures using Anguilliform-inspired robots. Hence the major contribution of this paper is the development of a framework for the determination of hydrodynamic parameter which can be further incorporated for motion prediction [2].

The physical experiments reported in this paper were conducted on an in-house developed Anguilliform-inspired robot. A proportional controller was employed which determined the required offset in an eel-like gait [9, 16] for tracking a commanded waypoint. Physical experiments were conducted in which the robot was programmed to follow specified waypoints for a range of gait parameters namely amplitude, frequency, phase-shift, and high-level controller gain. The corresponding trajectories followed by the robot were then recorded. The parameter estimation problem was further formulated as an optimization problem wherein the objective was to minimize the maximum of the difference between the robot trajectories obtained from the physical experiments and the simulations. The hydrodynamic parameters were then determined by solving the optimization problem and then tested using several test cases corresponding to the physical experiments conducted for different gait parameter combinations than the ones used for optimization.

A number of physical experiments were performed in which the robot was operated at four different amplitudes and four different frequencies. For all the sixteen combinations of amplitudes and frequencies, the robot was commanded to follow straight as well as turning motion. For straight motion, the waypoint was set at the distance of 1.40 m and at an angle of 0° with the X-axis of the global frame of reference. Similarly, for turning motion the waypoint was set at the distance of 1.40 m and at the angles of 30° with the X-axis of the global frame of reference. Out of the experiments conducted for sixteen gait parameter combinations, four were used as training set for determining the hydrodynamic parameters while the remaining twelve cases were used for testing/validating the estimated hydrodynamic parameters. The trajectory obtained in each of the aforementioned twenty-four experiments was compared with that of the one obtained from the developed simulator utilizing the estimated hydrodynamic parameters to validate the developed approach. This paper also reports two additional multi-waypoint following physical experiments.

2 Related Works

A detailed review of various fish-inspired robot designs has been reported by [17]. The problem of hydrodynamic parameter estimation for an Anguilliform-inspired robot involves two important aspects, namely, dynamics motion modeling and the techniques for hydrodynamic parameter estimation.

2.1 Dynamics Motion Models for Fish-Inspired Robots

In addition to the two-way coupling between the robot body and the surrounding fluid, the problem of dynamics motion modeling of the Anguilliform-inspired robot is complicated by the hyper-redundancy. Computational Fluid Dynamics (CFD) has been used to solve this problem [18, 19]. Although the solutions obtained by CFD have high accuracy, this method has high computational cost and hence cannot be directly used in motion planning and control of robots. To overcome this challenge various faster approaches have been developed which are based on Lighthill's model [20–22] and Morison's equation [23]. In these approaches, slender body, potential flow models and viscous friction models are used for improving the computational performance, however, at the cost of reduced accuracy.

Boyer et al. presented an extension of Lighthill's large amplitude elongated body theory (LAEBT) by adding resistive and axial forces that were neglected in the LAEBT for 3D swimming [24, 25]. They also approximated the

effects of the fluid viscosity on the motion of the body. Ramananarivo et al. used Lighthill's model to compute thrust force and thereby the swimming speed of the robot [26]. Porez et al. presented a dynamics model for a serially connected mobile multibody system based on the adaptation of LAEBT [27]. They further used Newton-Euler based algorithm to solve the forward dynamics of the robot. Clark et al. [28] and Wang et al. [29] used LAEBT based dynamics model developed by Wang et al. [30] to determine the hydrodynamic forces acting on a fish robot while performing locomotion.

Khalil et al. determined contact forces between fluid and links of the robot based on Morison's model [31]. Apneseth et al. made use of Morison's equation for finding the motion and acceleration of an articulated eel-like robot [32]. Kelasidi et al. also made use of Morison's equations along with the slender body assumption [9, 33]. Kopman et al. used Morison's equation to take into account the effect of the surrounding fluid on the robot body while performing locomotion [34].

The drag force acting on the robot body was determined based on quadratic drag model, according to which the drag force is proportional to the square of the forward velocity of the robot [10–13, 35–37]. Kanso et al. presented a motion model for swimming in a potential flow [38].

In a nutshell, the literature suggests that for low Reynolds number flows, Lighthill's resistance model is suitable while for high Reynolds number flows, Lighthill's reaction model based on the theory of slender body is suitable [39]. For moderate Reynolds number flows Morison's equation is most suitable [25]. Often, the slender body assumption and the use of irrotational and inviscid fluid flow in the motion models introduces a number of unknown hydrodynamic parameters. If the hydrodynamic parameters are not estimated properly then a large discrepancy between the model and the physical experiments may occur.

2.2 Hydrodynamic Parameter Estimation

In order to obtain an acceptable agreement between the output of the motion model and the physical robot motion, the coefficients used in the model need to be estimated. Several theoretical estimates have been reported by Kelasidi et al. [9] and Guskova et al. [14]. However, it has been reported that the parameters used are approximate and must be estimated via experiments [9].

Ranganathan et al. presented a framework for the estimation of hydrodynamic parameters of an underwater system via a mathematical model of the system involving the hydrodynamics of the system and the dynamics of the actuator and experiments [40]. They presented an iterative approach that utilizes the properties of least squares estimation algorithm along with free decay experiments to identify the system.

To determine the drag coefficients, Chen et al. performed several experiments wherein they pulled the robot at different speeds using a string attached to the robot at one end and to a motor at the other and determined the drag force acting on the robot via metric spring scales [41]. They used the determined drag to establish a relationship between drag force and velocity and used a least-squares method to determine the drag coefficient. Chan and Kang performed a similar experiment to determine the drag coefficients [42]. However, they immersed the robot in water and pulled the robot via string using external forces provided by different weights. The displacement-time data was recorded using an optical encoder and was compared with a theoretical model to determine the drag coefficients. Raj et al. also presented a similar method, however, the hydrodynamic parameters were determined via an optimization-based approach, wherein a match between displacement time data obtained via simulations and experiments was presented [43].

Phamduy et al. used a Blazka-type water tunnel to measure the flow of water upstream when the robot was placed in the tunnel at a fixed position [44]. The drag force acting on the robot was determined by using a load cell. They then used the classical drag equation [45] to determine the drag coefficient. Ramananarivo et al. determined the drag coefficient to minimize the squared difference between the experimental and simulated motion over a finite time period for a real fish [26].

For an Anguilliform-inspired robot with multiple joints, the tunnel experiments and the string-pulling experiments may result in relative movement of the joints, which may affect the accuracy of determination of these coefficients. Using a single link for the determination of these parameters may result in inaccurate measurement as all the different links may have different shapes; also the joints may affect the values of the drag coefficients.

In the field of Unmanned Surface Vehicles (USV) and Autonomous Underwater Vehicle (AUV) the parameters are estimated using free-running experiments by minimizing the error between the known parameters of the vehicle predicted by the dynamic model and the actual parameter values [46, 47]. Different algorithms used to reduce this difference include least squares [46, 48–50] and Least Squares Support Vector Machines (LS-SVM) [51, 52], Extended Kalman Filter (EKF) [53], and Prediction Error Method (PEM) optimization techniques [50]. Eng et al. [54] used State Variable Filter and Recursive Least Square (SVF-RLS) estimator in the training phase to estimate

the unknown parameters and then checked the validity of the results using fresh data. Other used methods include captive model experiments [55, 56] and Computational Fluid Dynamics (CFD) based simulation methods [55, 57].

The complexity of determination of the hydrodynamic parameters increases when the robot body has a hyper-redundant structure as in the case of Anguilliform-inspired robots. Kelasidi et al. developed a curve-fitting approach for the determination of the hydrodynamic parameters for underwater snake robot wherein they found the positions of the center of mass of the robot for a given combination of amplitude, frequency, phase-shift, and high-level controller gain and fit a curve between the experimental data and the simulation data to determine the hydrodynamic parameters [1]. However, the reported validation experiments were demonstrated for simple straight-line following. It is to be noted that in order to develop motion prediction capabilities, the error between the trajectories obtained from the experiments and the simulations must be minimized. The motion prediction capabilities, thus developed, can be used in localization, collision detection, and model predictive motion planning.

3 Problem Statement and Approach Overview

Given,

(i) an Anguilliform robot R with N links L_i, of length $2l$ each, serially connected via $N-1$ revolute joints J_j,

(ii) positions $\mathbf{p_i} = [p_{x_i}, p_{y_i}]^T$ of the centers of mass and orientations θ_i of links L_i expressed in the inertial frame of reference Ω,

(iii) the parametric motion model of R,

$$\dot{\mathbf{x}} = \mathbf{f}(\mathbf{x}, \boldsymbol{\tau}, \mathbf{v_c}; \mathbf{G_p}, \mathbf{e}), \tag{1}$$

where $\mathbf{x} = [\boldsymbol{\theta}, \mathbf{x_{CM}}, \dot{\boldsymbol{\theta}}, \dot{\mathbf{x}_{CM}}]^T$, $\boldsymbol{\theta} = [\theta_1, ..., \theta_n]^T \in \mathbb{S}^n$, θ_i is the orientation of the i^{th} link of the robot, $\bar{\theta} \in \mathbb{S}^1$ is the robot orientation and is determined as the heading angle of the robot $\bar{\theta} = \frac{1}{n}\sum_{i=1}^{n}\theta_i$, $\mathbf{x_{CM}} \in \mathbb{R}^2$ is the robot position and is determined as the center of mass of the robot $\mathbf{x_{CM}} = \frac{1}{n}\sum_{i=1}^{n}\mathbf{p_i}$, $\boldsymbol{\tau} = [\tau_1, ..., \tau_{n-1}]^T$ is the controlling joint torque vector used for servoing the joint motors to a commanded position, $\mathbf{v_c} = [v_x, v_y]^T = [s_c \cos\theta_c,\ s_c \sin\theta_c]^T$ is the velocity of the flow expressed in inertial frame Ω, s_c is the magnitude of the flow and θ_c is the direction of the flow expressed in the frame Ω and both the magnitude and direction of the flow are assumed to be steady, $\mathbf{G_p}$ is the gait parameter, $\mathbf{e} = [C_f, C_d, C_a, C_m]$ is the hydrodynamic parameter where C_f is the coefficients of drag force in the longitudinal direction, C_d is the coefficients of drag force in the transverse direction, C_a is the added mass coefficient, and C_m is the added inertia coefficient,

(iv) $\alpha_j = A_j \sin(\omega t + \beta_j) + \gamma$ be the desired joint angles following which R can reach to a commanded goal location $\mathbf{x_{CM,g}}$ (see Fig. 1), computed using an Eel-like gait generator [9] where the gait parameters are $A_j = A\frac{N-j}{N+1}$ which is the amplitude of oscillation of the jth joint, ω is the joint frequency, $\beta_j = (j-1)\beta$ is the phase-shift at joint j, A and β are parametric constants describing the amplitudes and phase-shifts, γ is the offset determined using a proportional controller, $\mathbf{G_p} = [A, \omega, \beta, k_\theta]$ denotes a specific gait parameter,

(v) set $\zeta = \{\mathbf{G_{p,1}}, \mathbf{G_{p,2}}, ...\mathbf{G_{p,q}}\}$ of q operating gait parameters,

(vii) training gait parameter set $\zeta_{train} \subset \zeta$,

(viii) testing gait parameter set $\zeta_{test} \subset \zeta$,

(ix) trajectory $(\mathbf{x_{CM}^{exp}}, \dot{\mathbf{x}}_{\mathbf{CM}}^{\mathbf{exp}})|_{\mathbf{G_p}}$ obtained from experiments and trajectory $(\mathbf{x_{CM}^{sim}}, \dot{\mathbf{x}}_{\mathbf{CM}}^{\mathbf{sim}})|_{\mathbf{G_p}}$ obtained from the simulations (see (iii) and (iv)), where $\mathbf{x_{CM}^{exp}}$ and $\mathbf{x_{CM}^{sim}}$ are the positions and $\dot{\mathbf{x}}_{\mathbf{CM}}^{\mathbf{exp}}$ and $\dot{\mathbf{x}}_{\mathbf{CM}}^{\mathbf{sim}}$ are the velocities on the robot trajectory determined from the physical experiments and the simulations respectively.

The objective is to determine the hydrodynamic parameters corresponding to straight and turning robot motions

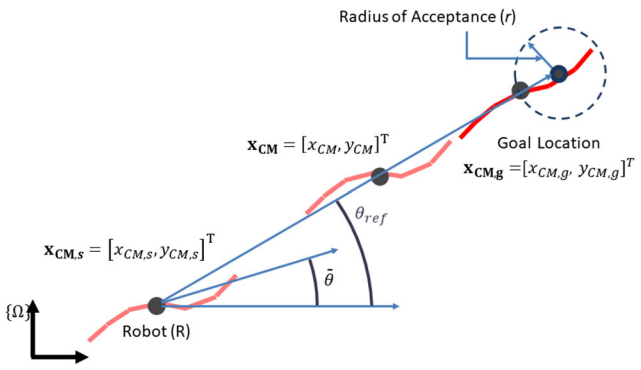

Fig. 1 Locomotion of an Anguilliform-inspired robot from the given start location $\mathbf{x_{CM,s}}$ to the goal location $\mathbf{x_{CM,g}}$ with a circle of acceptance of radius r

referred to in this paper as $\mathbf{e_1^*}$ and $\mathbf{e_2^*}$, respectively. The hydrodynamic parameters $\mathbf{e_1^*}$ and $\mathbf{e_2^*}$ can be determined by minimizing the maximum of the differences between the robot trajectories obtained from the physical experiments and the simulations for the test trajectories corresponding to the gait parameters belonging to the training set ζ_{train} for straight and turning robot motions, respectively.

The difference between the robot trajectories obtained from a physical experiment and the corresponding simulation can be determined by first sampling the trajectories and finding out the weighted sum of the absolute differences between the velocities and the positions at the sampled points.

Mathematically, $\mathbf{e_i^*}$ (i=1 and i=2) is determined such that,

$$\mathbf{e_i^*} = \underset{\mathbf{e_i}}{\operatorname{argmin}}[(\max_{j}(error_i(\mathbf{G_{p,j}})))] \tag{2}$$

where $\mathbf{G_{p,j}} \in \zeta_{train}$, $j = 1, ..., card(\zeta_{train})$, $card(\zeta_{train})$ is the number of training cases,

$$error_i(\mathbf{G_{p,j}}) = p_{error} + w v_{error}. \tag{3}$$

The term p_{error} is determined as follows:

$$p_{error} = \sum_{k=1}^{n} ||\mathbf{x_{CM,k}^{exp}} - \mathbf{x_{CM,k}^{sim}}|| \tag{4}$$

and denotes the total error in the estimation of the positions on the robot trajectories obtained from the physical experiments and the simulations.

The term v_{error} is determined as follows:

$$v_{error} = \sum_{k=1}^{n} ||\dot{\mathbf{x}}_{\mathrm{CM,k}}^{\mathrm{exp}} - \dot{\mathbf{x}}_{\mathbf{CM,k}}^{\mathbf{sim}}|| \tag{5}$$

and denotes total error in the estimation of the velocities on the robot trajectories obtained from the physical experiments and the simulations, $\mathbf{x_{CM,k}^{exp}}$ and $\mathbf{x_{CM,k}^{sim}}$ are k^{th} positions, $\dot{\mathbf{x}}_{\mathrm{CM,k}}^{\mathrm{exp}}$ and $\dot{\mathbf{x}}_{\mathbf{CM,k}}^{\mathbf{sim}}$ are the k^{th} velocities on the robot trajectory determined from the physical experiments and the simulations respectively, n is the number of points sampled on the robot trajectory, and w is a weighting parameter used for the optimization. It should be noted that $\mathbf{x_{CM,k}^{sim}}$ and $\dot{\mathbf{x}}_{\mathbf{CM,k}}^{\mathbf{sim}}$ can be obtained by solving the discretized parametric motion model (1). Also, numerically (1) is parameterised in terms of drag and added mass parameters C_f, C_d, C_a and C_m, which for convenience can be represented using hydrodynamic parameter vector $\mathbf{e} = [C_f, C_d, C_a, C_m]$. The objective is to determine $\mathbf{e}$ that satisfies (2). It is to be noted that the suffix i of $\mathbf{e}$ specifies that the hydrodynamic parameter corresponds to straight robot motion if $i = 1$ and turning motion if $i = 2$. Fitness function makes use of the 2-norm as 1-norm is more prone to sensing noise as compared to 2-norm.

In order to solve the problem of hydrodynamic parameter estimation outlined in Eq. 2, following approach was incorporated.

(i) A physical experimental setup comprising of an Anguilliform-inspired robot and a vision-based localization system was developed.
(ii) A simulator based on the model developed by [58] was implemented while incorporating the effects of localization and communication latency.
(iii) Physical waypoint following experiments for each gait parameter in ζ were performed and the corresponding trajectories were recorded.
(iv) An optimization problem for minimizing the maximum of the differences between the trajectories corresponding to ζ_{train} determined by the physical experiments and simulations was formulated and solved using Genetic Algorithm (GA) to determine the hydrodynamic parameters corresponding to both straight and turning robot motions.
(v) The estimated hydrodynamic parameters were validated on ζ_{test}.

In the following sections, each of the aforementioned step has been explained in details.

4 Experimental Setup

Figure 2a shows Anguilliform-inspired robot developed in our laboratory.

The dimensions of the robot are designed by taking inspiration from the anatomy of eels which have an elliptical cross-section with pointed tail fin. The robot is fabricated via a combination of rapid prototyping and laser cutting [59]. The entire body of the Anguilliform-inspired robot generates a large amplitude undulation which increases from the head towards the tail. The design of the robot imparts anisotropic drag which helps in generating propulsion [58]. All the numerical experiments reported in this paper are based on its dimensions.

The robot has a head module, four identical body modules, and a pointed tail that are serially connected via servomotor actuated revolute joints (see Fig. 2b). Head module contains an Atmega328 based Arduino Nano controller board, an XBee transreceiver, an on-board 7.4V, 2200mAh Li-ion based rechargeable battery pack, and a servomotor. Each of the body modules contain one servomotor (see Fig. 2b) that actuates a single degree of freedom revolute joint. The actuating motor was selected

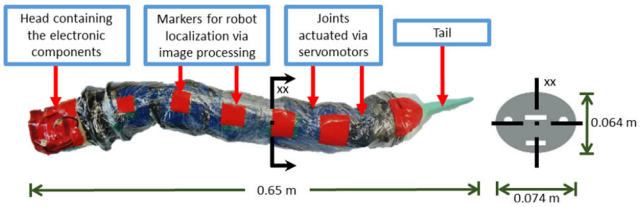

(a) Developed physical platform

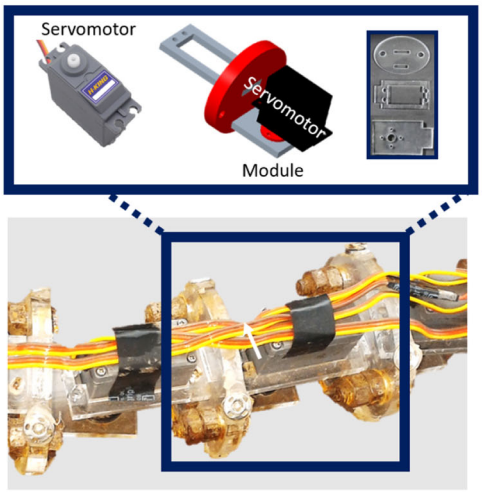

(b) Robot module

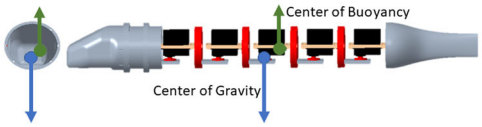

(c) Center of gravity and center of buoyancy of the robot.

Fig. 2 Anguilliform-inspired robot developed at MICL, IIT Patna

based on availability to be 12.8 kg-cm (1.26 N-m). The robot modules were designed to be of elliptical cross-section based on eel anatomy and the dimensions were so designed that the motor can be contained within. Further, the maximum moment to be generated by the motion to overcome drag was found to be 0.09 N which was much smaller than the available motor torque. The selected servomotor had a maximum angular velocity of 8 rad/s operational at 6 V. The power consumption per motor, therefore, was about 10 W. The robot specifications have been summarized in Table 1.

The developed robot was negatively buoyant and hence capable of swimming just below the surface of the water. Figure 2c shows the center of gravity and center of buoyancy of the robot when the robot lies still in the water. Currently, the robot can operate just below the water surface and can perform 2D motion. However, in the future, pectoral fins

Table 1 Robot specifications

Length of the robot	0.65 m
Major Diameter (2a)	0.074 m
Minor Diameter (2b)	0.064 m
Mass of the robot	1.75 kg
Number of links	6
Degrees of freedom	5

can be added to make the robot move deep into the water and thereby perform 3D motion.

Figure 3 shows the experimental setup used for waypoint following. The setup consists of an overhead camera which is used to localize the robot. For the overhead camera, a pixel of the acquired image represents 0.0038 m. Thus, the accuracy of the vision system was ±0.0019 m. A desktop computer was used to send the values of the gait parameters which include the amplitude, frequency, phase-shift and the high-level controller gain. These parameters were sent wirelessly via XBee module which has a communication frequency of 2.4 GHz.

A water pump with a flow rate of 0.0004 m^3/s and outlet pressure of 2.1×10^5 Pa was employed for generating the flow in the setup. The flow at the outlet of the pump was distributed into two outlet pipes each of length 1.5 m as shown in Fig. 3. Holes of diameter 7 mm were drilled at an equal spacing in each of these pipes in order to develop a uniform unidirectional ambient flow having a maximum magnitude of 0.08 m/s in the tank. A suction pipe was used

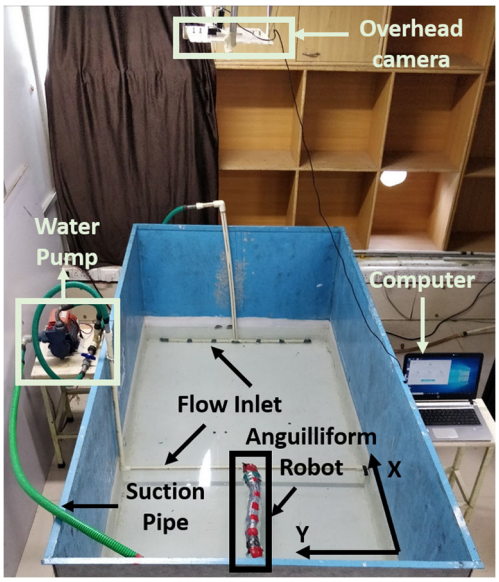

Fig. 3 Experimental setup

for creating low pressure near the inlet and thereby inducing flow in the tank.

5 Modeling and Simulation

5.1 Motion Modeling

The kinematics of Anguilliform-inspired robots are often represented using N-link swimmer model having $N-1$ revolute joints (see Fig. 4) [16, 23]. The forces acting on the Anguilliform robot include the linear and the nonlinear drag forces (resistive fluid forces), the added mass effect (reactive fluid forces), the fluid moments and effects due to ambient flow [16].

Let us suppose that the centroid of the i^{th} link is located at $\mathbf{p_i} = [x_{CM,i}, y_{CM,i}]^T$ and oriented θ_i radians with respect to the global frame of reference Ω where $i = 1, ..., N$, and α_j be the joint angles where $j = 1, ..., N-1$. The motion model used in this paper is based on Morison's equation and Newton-Euler's method [16]. The parametric motion model is expressed in state-space form using Eq. 1.

Equations 6 is used to determine $\ddot{\mathbf{x}}_{\mathbf{CM}}$

$$\ddot{\mathbf{x}_{CM}} = -\mathbf{M_p}\begin{bmatrix} \mathbf{a^T}\mu_n\mathbf{S}_\theta^2 & -\mathbf{a^T}\mu_n\mathbf{S}_\theta\mathbf{C}_\theta \\ -\mathbf{a^T}\mu_n\mathbf{S}_\theta\mathbf{C}_\theta & \mathbf{a}^T\mu_n\mathbf{C}_\theta^2 \end{bmatrix}\mathbf{M_k} - \mathbf{M_p}\begin{bmatrix} -\mathbf{a^T}\mu_n\mathbf{S}_\theta\mathbf{C}_\theta & -\mathbf{a}^T\mu_n\mathbf{S}_\theta^2 \\ \mathbf{a}^T\mu_n\mathbf{C}_\theta^2 & \mathbf{a}^T\mu_n\mathbf{S}_\theta\mathbf{C}_\theta \end{bmatrix}\begin{bmatrix} \mathbf{v_x^a} \\ \mathbf{v_y^a} \end{bmatrix}\dot{\theta} + \mathbf{M_p}\begin{bmatrix} \mathbf{a}^T\mathbf{f_{Dx}} \\ \mathbf{a}^T\mathbf{f_{Dy}} \end{bmatrix} \tag{6}$$

where,

$$\mathbf{M_k} = \begin{bmatrix} l\mathbf{K}^T(\mathbf{C}_\theta\dot{\boldsymbol{\theta}}^2 + \mathbf{S}_\theta\ddot{\boldsymbol{\theta}} \\ l\mathbf{K}^T(\mathbf{S}_\theta\dot{\boldsymbol{\theta}}^2 - \mathbf{C}_\theta\ddot{\boldsymbol{\theta}}) \end{bmatrix} \tag{7}$$

$$\mathbf{M_p} = \begin{bmatrix} m_{11} & m_{12} \\ m_{21} & m_{22} \end{bmatrix} = \begin{bmatrix} nm + \mathbf{a}^T\mu_n{\mathbf{S}_\theta}^2\mathbf{a} & -\mathbf{a}^T\mu_n\mathbf{S}_\theta\mathbf{C}_\theta\mathbf{a} \\ -\mathbf{a}^T\mu_n\mathbf{S}_\theta\mathbf{C}_\theta\mathbf{a} & nm + \mathbf{a}^T\mu_n{\mathbf{C}_\theta}^2\mathbf{a} \end{bmatrix}^{-1} \tag{8}$$

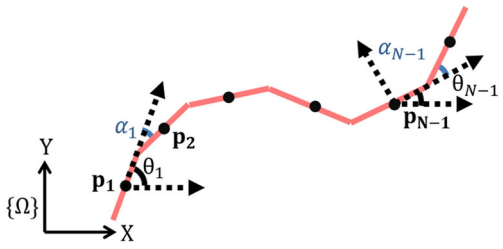

Fig. 4 Mathematical model of Anguilliform-inspired robot

and

$$\mathbf{a} = [1 \ldots 1]^T \in \mathbb{R}^N$$

The terms $\mathbf{F_{d_x}} = \mathbf{F_{dx}^I} + \mathbf{F_{dx}^{II}}$. $\mathbf{F_{d_y}} = \mathbf{F_{dy}^I} + \mathbf{F_{dy}^{II}}$ are drag forces in X and Y directions. $\mathbf{F_{dx}^I}$, $\mathbf{F_{dy}^I}$ and $\mathbf{F_{dx}^{II}}$, $\mathbf{F_{dy}^{II}}$ are the effects of linear and non-linear drag forces respectively.

$$\begin{bmatrix} \mathbf{F_{dx}^I} \\ \mathbf{F_{dy}^I} \end{bmatrix} = -\begin{bmatrix} c_t(\mathbf{C}_\theta)^2 + c_n(\mathbf{S}_\theta)^2 & (c_t - c_n)\mathbf{S}_\theta\mathbf{C}_\theta \\ (c_t - c_n)\mathbf{S}_\theta\mathbf{C}_\theta & c_t(\mathbf{S}_\theta)^2 + c_n(\mathbf{C}_\theta)^2 \end{bmatrix}\begin{bmatrix} \dot{\mathbf{p}_x} - \mathbf{v_x} \\ \dot{\mathbf{p}_y} - \mathbf{v_y} \end{bmatrix} \tag{9}$$

$$\begin{bmatrix} \mathbf{F_{dx}^{II}} \\ \mathbf{F_{dy}^{II}} \end{bmatrix} = -\begin{bmatrix} c_t\mathbf{C}_\theta & -c_n\mathbf{S}_\theta \\ c_t\mathbf{S}_\theta & c_n\mathbf{C}_\theta \end{bmatrix}\text{sgn}(\mathbf{v_{r_a}})\begin{bmatrix} {\mathbf{v_{r_x}}}^2 \\ {\mathbf{v_{r_y}}}^2 \end{bmatrix} \tag{10}$$

where

$$\mathbf{v_{r_a}} = \begin{bmatrix} \mathbf{v_{r_x}} \\ \mathbf{v_{r_y}} \end{bmatrix} = \begin{bmatrix} \mathbf{C}_\theta & \mathbf{S}_\theta \\ -\mathbf{S}_\theta & \mathbf{C}_\theta \end{bmatrix}\begin{bmatrix} \dot{\mathbf{p}_x} - \mathbf{v_x} \\ \dot{\mathbf{p}_y} - \mathbf{v_y} \end{bmatrix} \tag{11}$$

$$\mathbf{S}_\theta = \text{diag}(\sin\boldsymbol{\theta}), \sin\boldsymbol{\theta} = [\sin\theta_1 \ldots \sin\theta_N]^T \in \mathbb{R}^N \tag{12}$$

$$\mathbf{C}_\theta = \text{diag}(\cos\boldsymbol{\theta}), \cos\boldsymbol{\theta} = [\cos\theta_1 \ldots \cos\theta_N]^T \in \mathbb{R}^N \tag{13}$$

$$\mathbf{K} = \mathbf{A}^T(\mathbf{D}\mathbf{D}^T)^{-1}\mathbf{D} \tag{14}$$

$$\mathbf{V} = \mathbf{A}^T(\mathbf{D}\mathbf{D}^T)^{-1}\mathbf{A} \tag{15}$$

$$\mathbf{A} = \begin{bmatrix} 1 & 1 & & \\ & \ddots & \ddots & \\ & & 1 & 1 \end{bmatrix}_{(N-1)\times N} \tag{16}$$

$$\mathbf{D} = \begin{bmatrix} 1 & -1 & & \\ & \ddots & \ddots & \\ & & 1 & -1 \end{bmatrix}_{(N-1)\times N} \tag{17}$$

$\mathbf{v_x} = [v_{x,1}, \ldots, v_{x,N}]^T \in \mathbb{R}^N$, $\mathbf{v_y} = [v_{y,1}, \ldots, v_{y,N}]^T \in \mathbb{R}^N$, and $[v_{x,i}, v_{y,i}]^T$ is the flow velocity expressed in frame Ω. It is to be noted that the flow considered is an uniform ambient flow having velocity $\mathbf{v_c}$, hence, $v_{x,1} = v_{x,N} = \ldots v_{x,N} = s_c\cos(\theta_c)$ and $v_{y,1} = v_{y,N} = \ldots v_{y,N} = s_c\sin(\theta_c)$. $\mathbf{p_x} = [p_{x,1}, \ldots, p_{x,N}]^T$ and $\mathbf{p_y} = [p_{y,1}, \ldots, p_{y,N}]^T$, and $[p_{x,i}, p_{y,i}]^T$ is the position of the center of mass of each link in Ω. Coefficients $c_t = \frac{1}{2}\rho\pi C_f\frac{(b+a)}{2}2l$ and $c_n = \frac{1}{2}\rho C_d 2a2l$, are drag force parameters, ρ is the density of the fluid, $2l$ is the length of each link, $2a$ is the major diameter of the link, $2b$ is the minor diameter of the link, C_f is the coefficients of drag force in the longitudinal direction

and C_d is the coefficients of drag force in the transverse direction.

Link angular acceleration vector $\ddot{\boldsymbol{\theta}}$ can be determined using Eq. 18.

$$\ddot{\boldsymbol{\theta}} = \mathbf{M}_\theta{}^{-1}[\mathbf{D}^T\boldsymbol{\tau} - \mathbf{W}_\theta\dot{\boldsymbol{\theta}}^2 - \mathbf{V}_\theta\dot{\boldsymbol{\theta}} - \Lambda_\mathbf{3}|\dot{\boldsymbol{\theta}}|\dot{\boldsymbol{\theta}} - \mathbf{K_{Dx}}\mathbf{f_{Dx}} - \mathbf{K_{Dy}}\mathbf{f_{Dy}}] \tag{18}$$

where

$$\begin{aligned}\mathbf{M}_\theta &= \mathbf{J} + ml^2\mathbf{S}_\theta\mathbf{V}\mathbf{S}_\theta + ml^2\mathbf{C}_\theta\mathbf{V}\mathbf{C}_\theta + \Lambda_\mathbf{1} + l^2\mu_n\mathbf{K_1}\mathbf{K}^T\mathbf{S}_\theta \\ &\quad + l^2\mu_n\mathbf{K_2}\mathbf{K}^T\mathbf{C}_\theta\end{aligned} \tag{19}$$

$$\begin{aligned}\mathbf{W}_\theta &= ml^2\mathbf{S}_\theta\mathbf{V}\mathbf{C}_\theta - ml^2\mathbf{C}_\theta\mathbf{V}\mathbf{S}_\theta + l^2\mu_n\mathbf{K_1}\mathbf{K}^T\mathbf{C}_\theta \\ &\quad - l^2\mu_n\mathbf{K_2}\mathbf{K}^T\mathbf{S}_\theta\end{aligned} \tag{20}$$

$$\mathbf{V}_\theta = \Lambda_\mathbf{2} - l\mu_n\mathbf{K_2}\mathbf{V_x^a} - l\mu_n\mathbf{K_1}\mathbf{V_y^a} \tag{21}$$

$\mathbf{V_x^a} = \text{diag}(v_{x,1}, \ldots, v_{x,N}) \in \mathbb{R}^{N\times N}$, $\mathbf{V_y^a} = \text{diag}(v_{y,1}, \ldots, v_{y,N}) \in \mathbb{R}^{N\times N}$ and $\mu_n = \rho\pi C_a a^2 2l$,

$$\begin{aligned}\mathbf{K_{Dx}} &= l\mu_n m_{11}\mathbf{A_1}\mathbf{a}\mathbf{a}^T - l\mu_n m_{21}\mathbf{A_2}\mathbf{a}\mathbf{a}^T - l\mathbf{S}_\theta\mathbf{K} \\ \mathbf{K_{Dy}} &= l\mu_n m_{12}\mathbf{A_1}\mathbf{a}\mathbf{a}^T - l\mu_n m_{22}\mathbf{A_2}\mathbf{a}\mathbf{a}^T + l\mathbf{C}_\theta\mathbf{K}\end{aligned} \tag{22}$$

$$\begin{aligned}\mathbf{K_1} &= \mathbf{A_1} + \mu_n\mathbf{A_1}\mathbf{a}\mathbf{a}^T(m_{12}\mathbf{S}_\theta\mathbf{C}_\theta - m_{11}\mathbf{S}_\theta{}^2) \\ &\quad - \mu_n\mathbf{A_2}\mathbf{a}\mathbf{a}^T(m_{22}\mathbf{S}_\theta\mathbf{C}_\theta - m_{21}\mathbf{S}_\theta{}^2)\end{aligned} \tag{23}$$

$$\begin{aligned}\mathbf{K_2} &= \mathbf{A_2} - \mu_n\mathbf{A_1}\mathbf{a}\mathbf{a}^T(m_{11}\mathbf{S}_\theta\mathbf{C}_\theta - m_{12}\mathbf{C}_\theta{}^2) \\ &\quad + \mu_n\mathbf{A_2}\mathbf{a}\mathbf{a}^T(m_{21}\mathbf{S}_\theta\mathbf{C}_\theta - m_{22}\mathbf{C}_\theta{}^2)\end{aligned} \tag{24}$$

$$\mathbf{A_1} = \mathbf{S}_\theta\mathbf{K}\mathbf{S}_\theta{}^2 + \mathbf{C}_\theta\mathbf{K}\mathbf{S}_\theta\mathbf{C}_\theta \tag{25}$$

$$\mathbf{A_2} = \mathbf{S}_\theta\mathbf{K}\mathbf{S}_\theta\mathbf{C}_\theta + \mathbf{C}_\theta\mathbf{K}\mathbf{C}_\theta{}^2 \tag{26}$$

$\Lambda_\mathbf{1} = \lambda_1\mathbf{I_N}$, $\Lambda_\mathbf{2} = \lambda_2\mathbf{I_N}$ and $\Lambda_\mathbf{3} = \lambda_3\mathbf{I_N}$. The coefficients $c_t, c_n, \lambda_2, \lambda_3$ are drag force parameters, μ_n and λ_1 are added mass parameters, $\mathbf{J}{=}J\mathbf{I_N}$, $\mathbf{L} = l\mathbf{I_N}$, $\mathbf{M} = m\mathbf{I_N}$, $2l$ is the length of each link, m is the mass of each link, $J = \frac{1}{3}ml^2$ is the moment of inertia of each link and C_a is the added mass coefficient.

$$\lambda_1 = \frac{1}{12}\rho\pi C_m(a^2 - b^2)^2 l^3 \tag{27}$$

$$\lambda_2 = \frac{1}{6}\rho\pi C_f(a + b)l^3 \tag{28}$$

$$\lambda_3 = \frac{1}{8}\rho\pi C_f(a + b)l^4 \tag{29}$$

where C_m is the added inertia coefficient. It is to be noted that unlike terrestrial snake robots there is no similar non-holonomic kinematic constraint on their underwater counterparts. However, in order for it to generate propulsion, the robot structure has anisotropic drag which is implemented in the model using the coefficients C_f and C_d such that $C_f \neq C_d$ to ensure forward motion [58]. The terms $\dot{\mathbf{x}}_{CM}$ and $\dot{\boldsymbol{\theta}}$ can be obtained from Eqs. 6 and 18 by integrating $\ddot{\mathbf{x}}_{CM}$ and $\ddot{\boldsymbol{\theta}}$. Various other multi-body dynamics schemes have been developed and can also be used for developing the model for Anguillifrom-inspired robots [60, 61].

5.2 Motion Control

A two-layered control-architecture that includes a high-level proportional motion controller and a low-level PD controller has been employed (see Fig. 5). PD-based controller has been reported in the literature with a proof of stability in the case of Anguilliform-inspired robots by Kelasidi et al. [62] and hence has been chosen as the low-level controller.

For waypoint-following, the high-level proportional motion controller uses the reference heading angle generated based on a line-of-sight (LOS) guidance law to converge the robot's heading angle ($\bar{\theta}$) towards the reference heading angle (θ_{ref}) [63] (see Fig. 1).

The high-level controller determines the desired j^{th} joint angle α_j computed using an Eel-like gait generator [9] via (30) (see Fig. 5).

$$\alpha_j = A_j\sin(\omega t + \beta_j) + \gamma \tag{30}$$

where the gait parameters are $A_j = A\frac{N-j}{N+1}$ which is the amplitude of oscillation of the jth joint, ω is the joint frequency, and $\beta_j = (j-1)\beta$ is the phase-shift at joint j. A and β are parametric constants describing the amplitudes and phase-shifts, and γ is the offset determined using a proportional controller. Henceforth, the parameter A will be referred to as amplitude and β as the phase-shift in this paper.

The offset γ is determined using a proportional controller,

$$\gamma = k_\theta(\theta_{ref} - \bar{\theta}) \tag{31}$$

where k_θ is the high-level controller gain and θ_{ref} is the waypoint angle computed using Eq. 32.

$$\theta_{ref} = tan^{-1}\frac{y_{CM,g} - y_{CM}}{x_{CM,g} - x_{CM}} \tag{32}$$

where $\mathbf{x_{CM,g}} = [x_{CM,g}, y_{CM,g}]^T$ is the goal location and $\mathbf{x_{CM}} = [x_{CM}, y_{CM}]^T$ is the position of center of mass of the robot (see Fig. 1).

The low-level PD controller determines the required motor torque which allows the robot to achieve the desired heading angle. The joint torques are calculated from the reference joint angle α_j to control the link angles according to Eq. 33.

$$\boldsymbol{\tau} = k_p \mathbf{e}_\alpha + k_d \dot{\mathbf{e}_\alpha} \tag{33}$$

where $\mathbf{e}_\alpha = \boldsymbol{\alpha} - \boldsymbol{\alpha}^*$, $\boldsymbol{\alpha}^*$ is the actual joint angle, and k_p and k_d are proportional and derivative gains respectively. The gains k_θ, k_p and k_d are tuned manually. The process of estimation of the low-level gains has been provided in Supplementary Data 1. It should be noted that, for simplicity, PD controller has been employed in this paper. Any other non-linear controller [64–66], however, can be easily integrated into the developed framework.

5.3 Dynamics Simulation

A dynamics simulator which incorporates the model presented in Sections 5.1 and 5.2 has been developed and the details are provided in this section. The control frequency has been modeled in the developed simulator to account for the latency caused due to image processing based localization and wireless communication. The simulation time-step should always be smaller than the control time-step to capture the dynamics of the robot. The camera data is sampled at 30 fps i.e., with a sampling period of 0.033 s. The computations taking place during the execution of the high-level control-loop comprise of: 1) image acquisition, 2) image-based localization, 3) transmitting the desired joint angles via X-Bee, and 4) executing the commanded joint angles by the robot using the low-level control loop. The maximum computation time for the control time-step was experimentally found to be approximately 0.3 s which varies based on the availability of computational resources. The execution of the high-level control loop takes place after the completion of the execution of the low-level control loop, i.e. the joints reaching their respective commanded positions. The system remains stable because the completion of the low-level control loop execution is ensured by inserting a predetermined time-delay before the high-level control loop is executed.

To take into account the variations in the robot motion, the simulation time-step should be significantly small compared to the control time-step which has been experimentally found to be 0.3s. The simulation time-step depends upon the maximum robot speed, the flow speed, and the obstacle density. For the purpose of the reported robot and the test environment, the time-step was determined by trial-and-error to be 0.01 s.

The steps used in the simulation of the robot are enumerated below.

(i) $\boldsymbol{\tau}$ is determined using Eq. 33.
(ii) The values of $\ddot{\boldsymbol{\theta}}$ is further determined from Eq. 18. $\ddot{\boldsymbol{\theta}}$ is then used to calculate the values of $\boldsymbol{\theta}$ by using RK4.
(iii) $\ddot{\mathbf{x}}_{\mathbf{CM}}$ is determined from Eq. 6 and further RK4 is applied to determine $\mathbf{x}_{\mathbf{CM}}$.

This process is continued until $||\mathbf{x}_{\mathbf{CM,g}} - \mathbf{x}_{\mathbf{CM}}|| < r$ where r is the radius of acceptance. The length of an Anguilliform robot is large and therefore denoting a particular point on the robot as one representing the entire robot is incorrect. Hence it was assumed that if up to 23% of the body length has reached near the goal then the robot has reached the goal. Hence, the radius of acceptance is chosen to be approximately equal to 0.15 m (0.23 BL).

6 Waypoint-Following Experiments

Various physical experiments were performed in which the robot was operated at four different gait amplitudes (A = 0.61 rad, 0.69 rad, 0.78 rad, 0.87 rad) and frequencies (ω = 2.7 rad/s, 3.1 rad/s, 3.5 rad/s, 3.9 rad/s). Due to the physical constraints of the robot, the amplitude of oscillation of the links can vary from 0 degree (0 rad) to 50 degrees (0.87 rad). However, experimentally it was found that if the amplitude was less than 35 degrees (0.61 rad) then no forward motion was achieved by the robot. Hence, the gait amplitudes were discretized into four equal intervals in between 35 degrees (0.61 rad) and 50 degrees (0.87 rad). Similarly, for the frequencies less than 155 degrees/s (2.7 rad/s), no forward motion was achieved in the robot. Hence the frequencies were discretized into four equal intervals in between 2.7 rad/s and 3.9 rad/s.

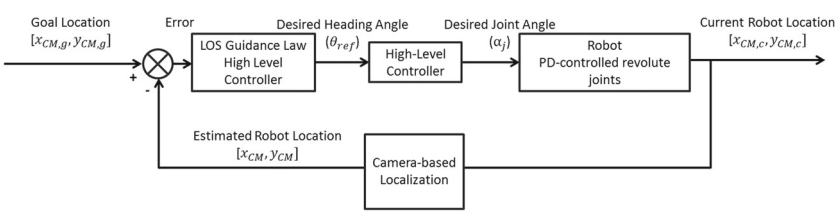

Fig. 5 The control scheme used to control the motion of the robot

The robot was commanded to follow straight and turning motion for each of the aforementioned sixteen combinations of gait amplitudes and frequencies. The waypoints were set at the distance of 1.40 m (2.2 BL) and at the angles of 0° (to represent straight motion) and 30° (to represent turning motion) to the global X-axis, respectively. Thus, thirty-two experiments were performed and the robot trajectories in each case were recorded. The value of phase-shift β was set as 1.04 rad for the aforementioned experiments. Also, the high-level controller gain k_θ for straight as well as turning motion were manually tuned and the determined values were 0.1 and 0.37 respectively. It should be noted that, a moving median filter was applied over the sensor data to remove the noise.

The four training cases ζ_{train} were selected by considering the physical experiments conducted for the extreme values of gait amplitude and frequency, i.e., (1) A = 0.61 rad, ω = 2.7 rad/s, (2) A = 0.61 rad, ω = 3.9 rad/s, (3) A = 0.87 rad, ω = 2.7 rad/s, and (4) A = 0.87 rad, ω = 3.9 rad/s. Hence, ζ_{train} = {[0.61, 2.7], [0.61, 3.9], [0.87, 2.7], [0.87, 3.9]}. The test cases used for validation of the estimated hydrodynamic parameters corresponding to the remaining twelve cases. Hence, ζ_{test} = {[0.61, 3.1], [0.61, 3.5], [0.69, 2.7], [0.69, 3.1], [0.69, 3.5], [0.69, 3.9], [0.78, 2.7], [0.78, 3.1], [0.78, 3.5], [0.78, 3.9], [0.87, 3.1], [0.87, 3.5]}.

The turning angle of 30° was selected based on the space constraints posed by the physical experimental setup. The developed framework, however, is flexible to incorporate more number of levels of turning.

7 Estimation of Hydrodynamic Parameters (C_f, C_d, C_a and C_m)

To estimate the hydrodynamic parameters, a training set ζ_{train} was considered for both straight and turning motion. The weight w corresponding to each element of ζ_{train} was set to 5. In each training case, the error in the trajectories obtained from the simulations and free-running physical experiments conducted for identical waypoints, gait parameters, and controller gains were determined.

The hydrodynamic parameter estimation problem was then formulated as the minimization of the objective function which was defined as the maximum error in the trajectories among the four test cases. A closed-form solution of the hydrodynamic parameters using a least-squares approach is not possible due to the implicit nature of the model. Hence, Genetic Algorithm (GA) based approach has been used for hydrodynamic parameter estimation.

The difference between the robot trajectories is computed by sampling points on the robot trajectories obtained from simulations and physical experiments and finding out the weighted sum of the absolute differences between the velocities and the positions at the sampled points obtained via simulations and experiments. The testing was then carried out for ζ_{test} for both straight and turning motion.

To determine the fitness functions, first the trajectories obtained from the physical experiments were sampled into n = 7 time intervals and the simulations and experiments were compared at the exactly same time stamps.

To have a check on the poor quality solutions, conditions were added in the fitness function to penalize extremely long travel times, ill-conditioned matrices, and self-collisions (see Eq. 34). The fitness function f_i was defined for both straight (i = 1) and turning motion (i = 2) as

$$f_i = \begin{cases} \max\limits_j(error_i(\mathbf{G_{p,j}})) & \text{if } t \le T_{max}, \\ H_1 L & \text{if } t > T_{max}, \\ H_2 & \text{if } M_\theta \text{ is an ill-conditioned matrix}, \\ H_3 & \text{if self-collision occurs}, \end{cases} \tag{34}$$

where t is the travel time required by the robot to reach the specified waypoint and T_{max} is the maximum allowable travel time for which the evaluation shall run. The conditions used in Eq. 34 have been explained in Table 2.

Table 2 Values of fitness under different conditions

Fitness Value	Condition
$\max\limits_j(error_i(\mathbf{G_{p,j}}))$	If the robot reaches the specified waypoint at time $t \le T_{max}$.
$H_1 L$	If the travel time required by the robot is more than T_{max} then the fitness value is set to $H_1 L$ where H_1 is a large number and L is the distance between robot position at T_{max} and the corresponding waypoint location.
H_2	From the dynamics, it can be seen that when the matrix M_θ (see Eq. 18) becomes ill-conditioned it leads to a poor solution. The rank of the matrix is determined to find its ill-conditioning. If the $rank(M_\theta) < N$ the fitness value is set to be H_2 which is a large number and N is the number of links of the robot.
H_3	If self-collision occurs.

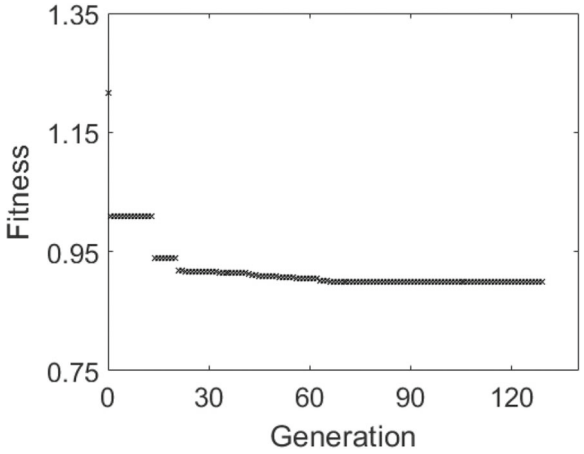

(a) Fitness versus generation for straight motion (The raw data comprising of the fitness values versus generations have been provided in Supplementary Data 2)

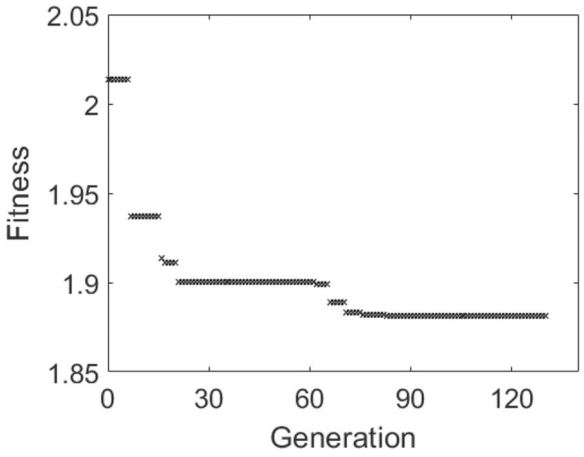

(b) Fitness versus generation for turning motion. (The raw data comprising of the fitness values versus generations have been provided in Supplementary Data 3)

Fig. 6 Fitness versus generation

The numerical values of H_1, H_2 and H_3 were set as 10^6, 10^{16} and 10^{14} respectively in the simulations reported in this paper. However, any set of large values satisfying the inequality $H_2 > H_3 > H_1$ may be used.

The inequalities between the values of H_1, H_2 and H_3 are determined based on the following considerations.

(i) H_2 is given the largest numeric value to severely penalize random solutions that may lead to ill-conditioned matrices during the evaluation of fitness function using simulations.
(ii) Self-collision, less preferred over long travel time, has been penalized more by setting the value of $H_3 > H_1$.

The fitness functions (see Eq. 34) were formulated for straight and turning motion, and the optimization problems were solved using Matlab's Genetic Algorithm (GA) toolbox. The computational complexity of estimation depends on the population size and the number of generations used. The population size was chosen as 150, while the optimization routine was executed over 130 generations (see Fig. 6). The crossover function used was 'scattered'.

GA was successfully converged for both straight and turning motion. The fitness evaluation of Genetic Algorithm (GA) was observed to reach a steady state which can be seen from the results of individual optimization (see Fig. 6). As the fitness reaches a steady state the solution is bound to reach a near-optimal condition. However, being a metaheuristic technique there cannot be a mathematical guarantee that the solution obtained by GA is optimal. Hence for the practical purpose near-optimal solution can be assumed to be acceptable.

Table 3 presents the values of hydrodynamic parameters obtained via optimization and the corresponding fitness values. A comparison of the positions of the robot along the trajectories obtained via the experiments and the simulations for ζ_{train} has been provided in Supplementary Data 4.

It is to be noted that due to the image-processing based measurement, uncertainties of ± 0.0019 m and ± 0.1 s in localization and estimation of time exists. The uncertainties in the determined hydrodynamic parameters have been, thus, estimated to be of the order of ± 0.0001.

8 Validation

In order to validate the estimated values of hydrodynamic parameters determined in Section 7, the trajectories

Table 3 Optimized hydrodynamic parameters for straight and turning robot motion

Motion	Optimized hydrodynamic parameters				Fitness value
	C_f	C_d	C_a	C_m	
Straight	0.008	0.776	0.618	0.007	0.8984
Turning	0.009	0.978	1.169	0.001	1.8814

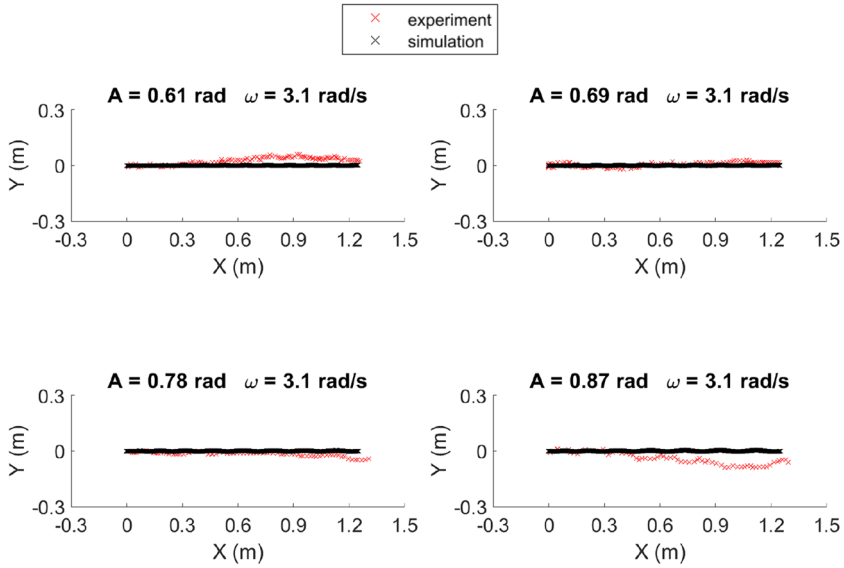

Fig. 7 Comparison of the positions of the robot along the trajectories obtained via experiments and simulations for straight motion

obtained from the experiments and the simulations were compared for ζ_{test} for both straight and turning motion.

8.1 Comparison of Robot Trajectories

The robot trajectories obtained via the experiments and the simulations for twelve test cases were compared for both straight and turning motion. Figures 7 and 8 shows the positions of the robot over the trajectories for four test cases ($A = 0.61$ and $\omega = 3.1$, $A = 0.69$ and $\omega = 3.1$, $A = 0.78$ and $\omega = 3.1$, and $A = 0.87$ and $\omega = 3.1$) each corresponding to the straight and the turning motions respectively. For brevity, the rest of the eight cases corresponding to the straight and the turning motions have been presented in Appendix A (see Figs. 12 and 13).

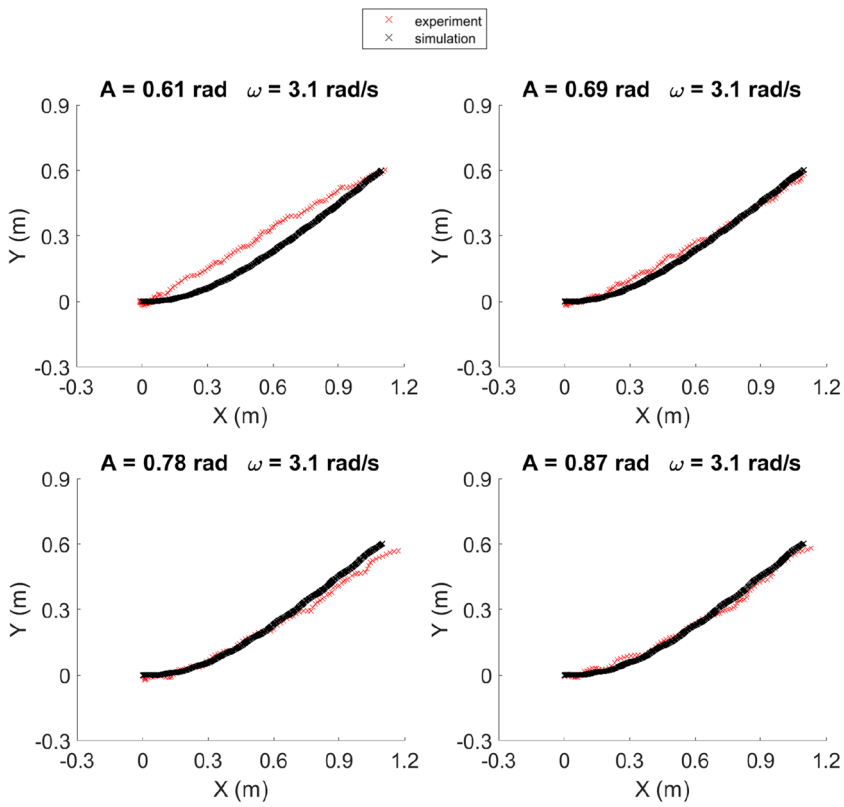

Fig. 8 Comparison of the positions of the robot along the trajectories obtained via experiments and simulations for turning motion

In four out of twelve cases (A = 0.61 and ω = 3.1, A = 0.69 and ω = 3.1, A = 0.69 and ω = 3.9, and A = 0.78 and ω = 2.7) for turning motion, it does appear that the paths obtained via the experiments are linear but in other cases it does go in a non-linear fashion based on which the observed linear paths may be considered to be a chance occurrence.

The root-mean square (RMS) errors E_x between the positions and the velocities sampled from the robot trajectories obtained via the simulations and the physical experiments for both straight and turning motions were determined using

$$E_x = \frac{1}{n}\sum_{k=1}^{n} ||(\mathbf{x}_{\mathbf{CM,k}}^{\mathbf{exp}} - \mathbf{x}_{\mathbf{CM,k}}^{\mathbf{sim}})|| \tag{35}$$

where, n = 35, $\mathbf{x}_{\mathbf{CM,k}}^{\mathbf{exp}}$ is the k^{th} sampled position on the robot trajectory determined from the physical experiments and $\mathbf{x}_{\mathbf{CM,k}}^{\mathbf{sim}}$ is the k^{th} sampled position on the robot trajectory determined from the simulations. E_x was computed for each gait parameter combination, and straight and turning motion.

Similarly, the RMS errors E_v in velocities were then computed using

$$E_v = \frac{1}{n}\sum_{k=1}^{n} ||(\dot{\mathbf{x}}_{\mathbf{CM,k}}^{\mathbf{exp}} - \dot{\mathbf{x}}_{\mathbf{CM,k}}^{\mathbf{sim}})|| \tag{36}$$

where, n = 35, $\dot{\mathbf{x}}_{\mathrm{CM,k}}^{\mathrm{exp}}$ is the k^{th} sampled velocity on the robot trajectory determined from the physical experiments and $\dot{\mathbf{x}}_{\mathbf{CM,k}}^{\mathbf{sim}}$ is the k^{th} sampled velocity on the robot trajectory determined from the simulations. E_v was computed for each gait parameter combination, and for straight and turning motion.

The consistency and the accuracy of the estimated parameters were determined based on the RMS errors between the positions and velocities over the trajectories obtained via the simulations and the experiments. From Figs. 7, 8, 12 and 13 it can be seen that the variations between the simulation and the experimental trajectories are random.

Table 4 shows the RMS errors E_x and E_v corresponding to the positions and velocities respectively obtained for the testing cases.

The RMS error in positions depends upon the accuracy of the experimental runs and the radius of the circle of acceptance which is 0.23 BL. Thus, the RMS error below 0.23 BL is acceptable. A maximum RMS error in the position of 0.082 BL and 0.183 BL were obtained for straight and turning motions respectively and are hence acceptable. Similarly, a maximum RMS error in velocities of 0.03 BL/s and 0.02 BL/s were obtained for straight and turning motion respectively and is acceptable. Hence, the determined parameters are consistent over the gait parameter range.

8.2 Multi-waypoint Following Experiments

To validate the obtained values of the hydrodynamic parameters, a comparison was made between the simulations and the physical experiments wherein the robot was commanded to follow a path comprising of a sequence of waypoints. This section presents the results of the comparison of the trajectories obtained from the simulations and the experiments for two such paths comprising of a sequence of three waypoints each. The gait parameters in the reported experiments and simulations were set as A = 0.87 rad, ω = 3.9 rad/s, β = 1.04 rad, and k_θ = 0.37.

Path 1: The robot was initially placed at (0.00 m, 0.00 m) and was commanded to follow a path comprising of a

Table 4 RMS errors for testing cases for different gait parameters, and for straight and turning motion

Gait parameters		Straight motion		Turning motion	
Amplitude (rad)	Frequency (rad/s)	E_x (BL)	E_v (BL/s)	E_x (BL)	E_v (BL/s)
0.61	3.1	0.034	0.01	0.136	0.02
	3.5	0.060	0.02	0.100	0.01
0.69	2.7	0.029	0.02	0.183	0.02
	3.1	0.016	0.01	0.069	0.01
	3.5	0.024	0.01	0.135	0.02
	3.9	0.025	0.01	0.112	0.01
0.78	2.7	0.082	0.03	0.154	0.02
	3.1	0.022	0.02	0.051	0.02
	3.5	0.034	0.02	0.179	0.02
	3.9	0.074	0.02	0.145	0.02
0.87	3.1	0.040	0.03	0.159	0.02
	3.5	0.021	0.02	0.061	0.02

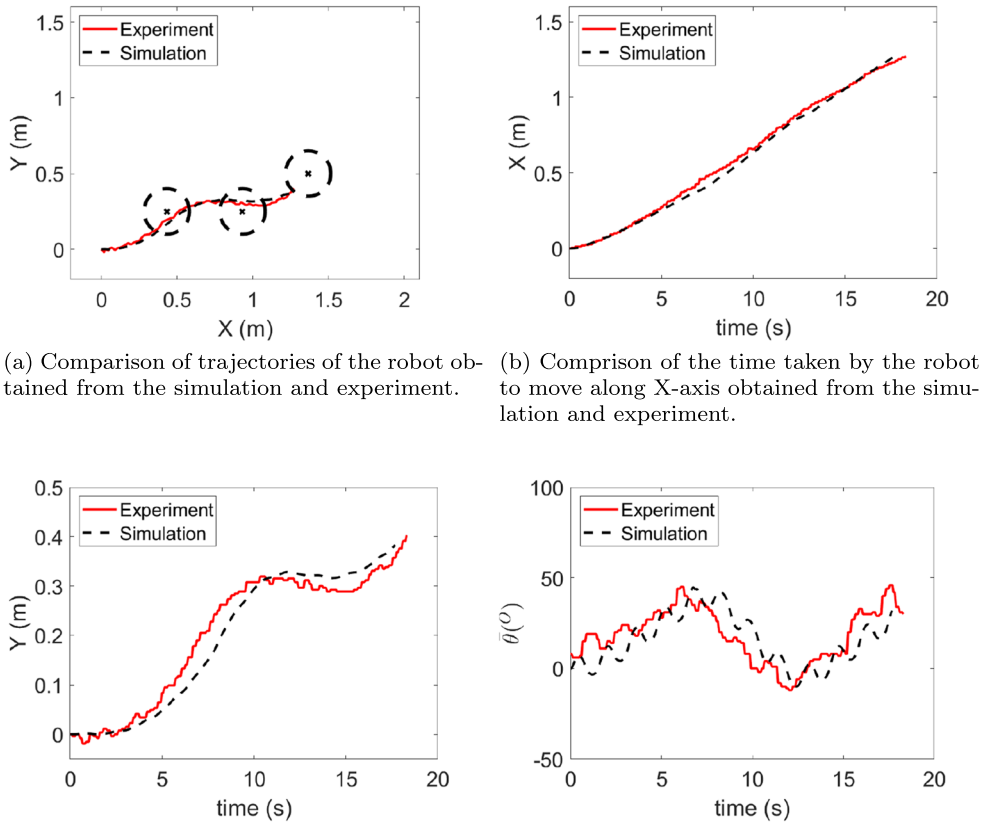

Fig. 9 Comparison of the robot trajectories obtained via simulation and physical experiment for path 1 (a video of this comparison can be found in Multimedia Extension 1)

(a) Comparison of trajectories of the robot obtained from the simulation and experiment.

(b) Comprison of the time taken by the robot to move along X-axis obtained from the simulation and experiment.

(c) Comprison of the time taken by the robot to move along Y-axis obtained from the simulation and experiment.

(d) Comprison of the heading angles of the robot over the trajectory obtained from the simulation and experiment.

sequence of three waypoints which were placed at (0.43 m, 0.25 m), (0.93 m, 0.25 m) and (1.37 m, 0.5 m) (see Fig. 3a). The RMS error between the positions over the trajectory obtained via simulation and experiment was 0.01 BL and the RMS error between the velocities over the trajectories obtained via simulation and experiment was 0.005 BL/s. Figure 9b and c show the variation of x-coordinates and y-coordinates with time obtained via the experiments and simulations for Path 1. Figure 9d show the comparison of the variation of the heading angle with respect to time obtained via experiments and simulations for Path 1.

Path 2: The robot was initially placed at (0.00 m, 0.00 m) and was commanded to follow a path comprising of a sequence of three waypoints which were placed at (0.35 m, 0.2 m), (0.69 m, 0.4 m), and (1.07 m, 0.4 m) under influence of ambient flow of magnitude 0.03 m/s (0.05 BL/s) acting along 180° to the global X-axis (see Fig. 10a). The RMS error between the positions over the trajectory obtained via simulation and experiment was 0.01 BL and the RMS between the velocities over the trajectory obtained via simulation and experiment was 0.004 BL/s. Figure 10b and c show the variation of x-coordinates and y-coordinates with time obtained via the experiments and simulations for Path 2. Figure 10d show the comparison of the variation of the heading angle with respect to time obtained via experiments and simulations for Path 2.

To estimate the effects of variation in inputs, a number of waypoint following experiments were considered. While following the waypoints, the robot speed varies from 0 m/s to 0.093 m/s (0.14 BL/s) and it was found that trajectories were followed with a maximum RMS error in position of 0.31 BL and a maximum RMS error in velocity of 0.03 BL/s showing an acceptable level of deviation. Computation of errors for following multiple waypoints between the simulated and physical robot has not been reported earlier for Anguilliform-inspired robots.

8.3 Application of the Determined Hydrodynamic Parameters in Generation of Motion Primitives for Model Predictive Trajectory Planning

To demonstrate the application of motion prediction, an example of motion planning employing model predictive path planning approach has been presented. In this example, the simulated Anguilliform-inspired robot is commanded to reach a specified goal location while avoiding multiple obstacles wherein the goal is to determine a collision-free path between the start and the goal locations.

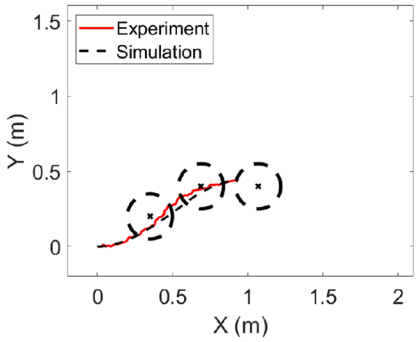

(a) Comparison of trajectories of the robot obtained from the simulation and experiment.

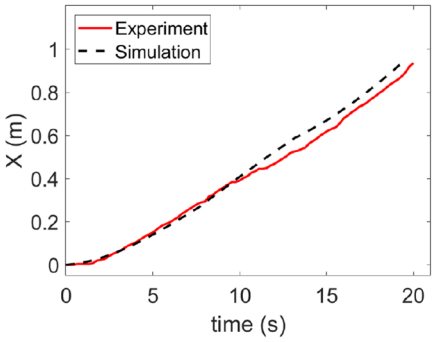

(b) Comprison of the time taken by the robot to move along X-axis obtained from the simulation and experiment.

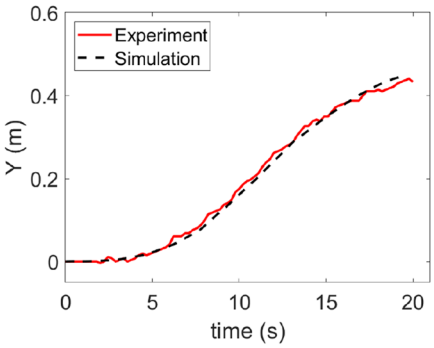

(c) Comprison of the time taken by the robot to move along Y-axis obtained from the simulation and experiment.

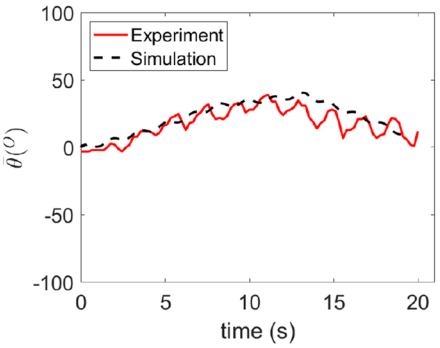

(d) Comprison of the heading angles of the robot over the trajectory obtained from the simulation and experiment.

Fig. 10 Comparison of the robot trajectories obtained via simulation and physical experiment under the influence of ambient flow acting along 180° to the global X-axis for path 2 (a video of this comparison can be found in Multimedia Extension 2)

To solve the problem of trajectory planning following steps are involved [2]:

(i) A dynamically feasible action set is generated using the dynamics simulator reported in this paper. The action sets are generated for discretized flow directions and waypoint pose. Figure 11a shows three actions corresponding to the flow acting along 0°. Similar actions are generated for all the discrete ambient flow direction which in the case of the example has been chosen to be eight, varying from 0° to 315°.

(ii) The generated action set is then used to compute motion primitives which are further used to develop a search-tree. To determine the regions of the possible collision for each of the actions, a convex hull around the region encompassed by the robot while executing the action is determined. Figure 11b shows the convex hulls obtained for eight discretized ambient flow directions. During the construction of the search-tree, the motion primitives are chosen based on the relative flow direction with respect to the orientation of the robot [2].

(iii) An admissible simulation-based heuristic is further designed to improve the computational performance of the robot.

(iv) Finally, search algorithms such as A*, D*, etc [2, 8, 67, 68] is used to determine a collision-free, dynamically feasible optimal trajectory between the specified start and the goal location.

9 Conclusion

This paper presents an optimization-based approach for the estimation of hydrodynamic parameters and the validation of the same on an in-house developed Anguilliform-inspired robotic platform. Fitness functions were designed for optimization as the maximum of the difference between the robot trajectories obtained from the experiments and the simulations for the test trajectories corresponding to the identical gait parameter set, for the straight and the turning motions. Penalties were incorporated for the occurrence of extremely long travel times, ill-conditioned matrices and self-collisions during the simulations into the fitness function.

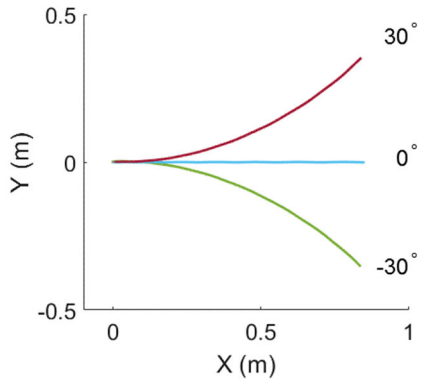

(a) Action set for flow along 0°

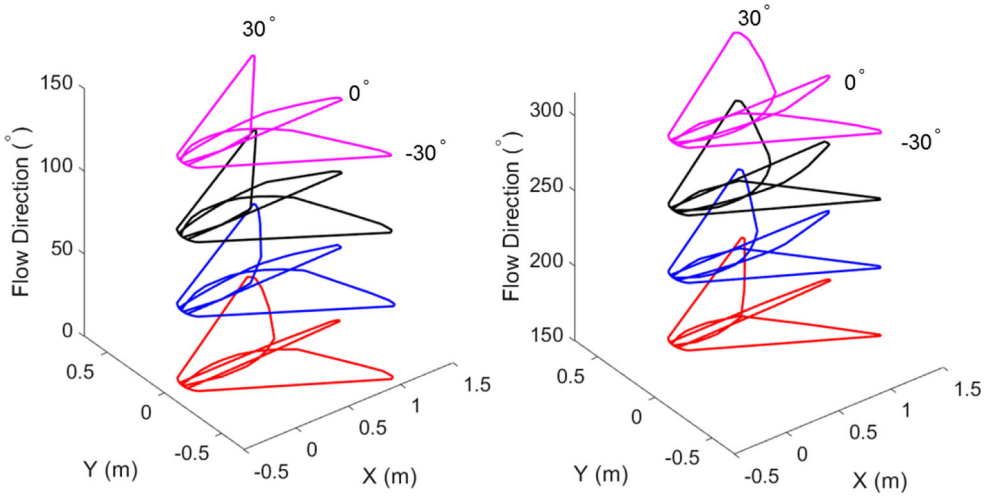

(b) Convex envelopes for different flow directions

Fig. 11 Model Predictive Trajectory Planning

The determined parameters were then tested on twenty-four different test cases, twelve for straight motion and twelve for turning motion (different from the eight training cases). Also, to validate the developed approach different experiments were performed. The maximum RMS error in the position of 0.082 BL and a maximum RMS error in the speed of 0.03 BL/s were obtained for the straight motion. Similarly, for the turning motion, a maximum RMS error in the position of 0.183 BL and a maximum RMS error in the speed of 0.02 BL/s were obtained. Hence, the determined parameters are consistent over different gait parameters. Compared to the literature [1], the reported approach has been validated for both straight and turning motions. Also, for a wider range of gait parameters and a more detailed comparison of trajectories obtained has been presented here instead of a simple comparison of average speeds.

The hydrodynamic parameters obtained by the developed approach are also validated by performing the experiments wherein the physical robot was commanded to follow multiple waypoints both in the absence and the presence of ambient flow. A close agreement between the trajectories obtained by the simulations and the experiments was found and the maximum RMS error between the positions over the trajectories obtained via simulations and experiments was 0.01 BL and the RMS error between the velocities over the trajectories obtained via simulations and experiments was 0.005 BL/s. Hence, the hydrodynamic parameters estimated via the approach reported in this paper can be used for predicting the robot trajectories using the simulation for any given sequence of waypoints with an acceptable level of fidelity both in the presence and in the absence of ambient flow.

The developed dynamics simulations incorporating the optimized hydrodynamic parameter can be further used in motion prediction and can be integrated with model predictive planning framework for dynamically feasible trajectory planning of Anguilliform-inspired robots [2] and has been presented via example in this paper.

Acknowledgments This research has been supported by the Department of Science and Technology (DST), Government of India [grant number SB/FTP/ETA-44/2013]. Opinions expressed are those of the authors and do not necessarily reflect the opinions of the sponsors.

Appendix A: Robot Trajectories Obtained via Experiments and Simulations for Straight and Turning Motion

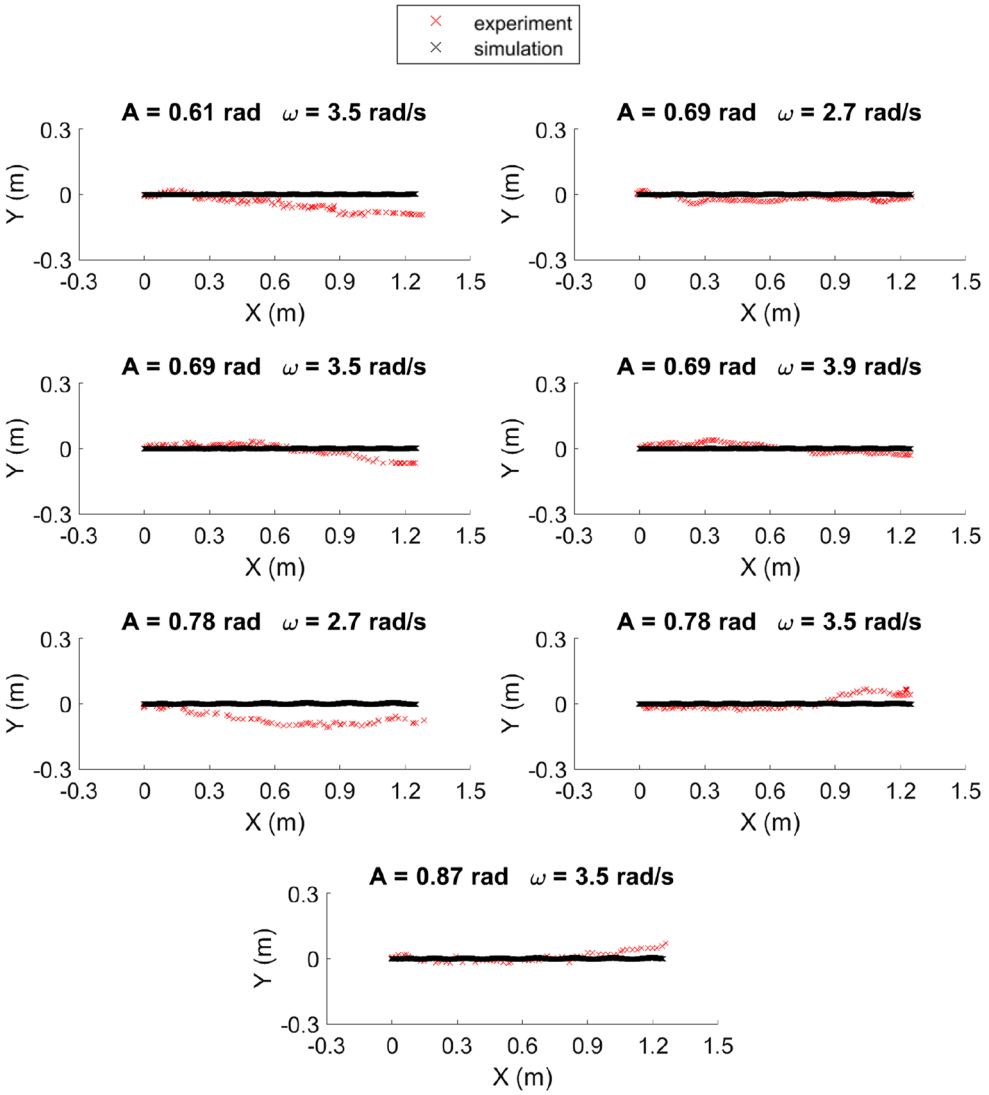

Fig. 12 Comparison of the positions of the robot along the trajectories obtained via experiments and simulations for straight motion

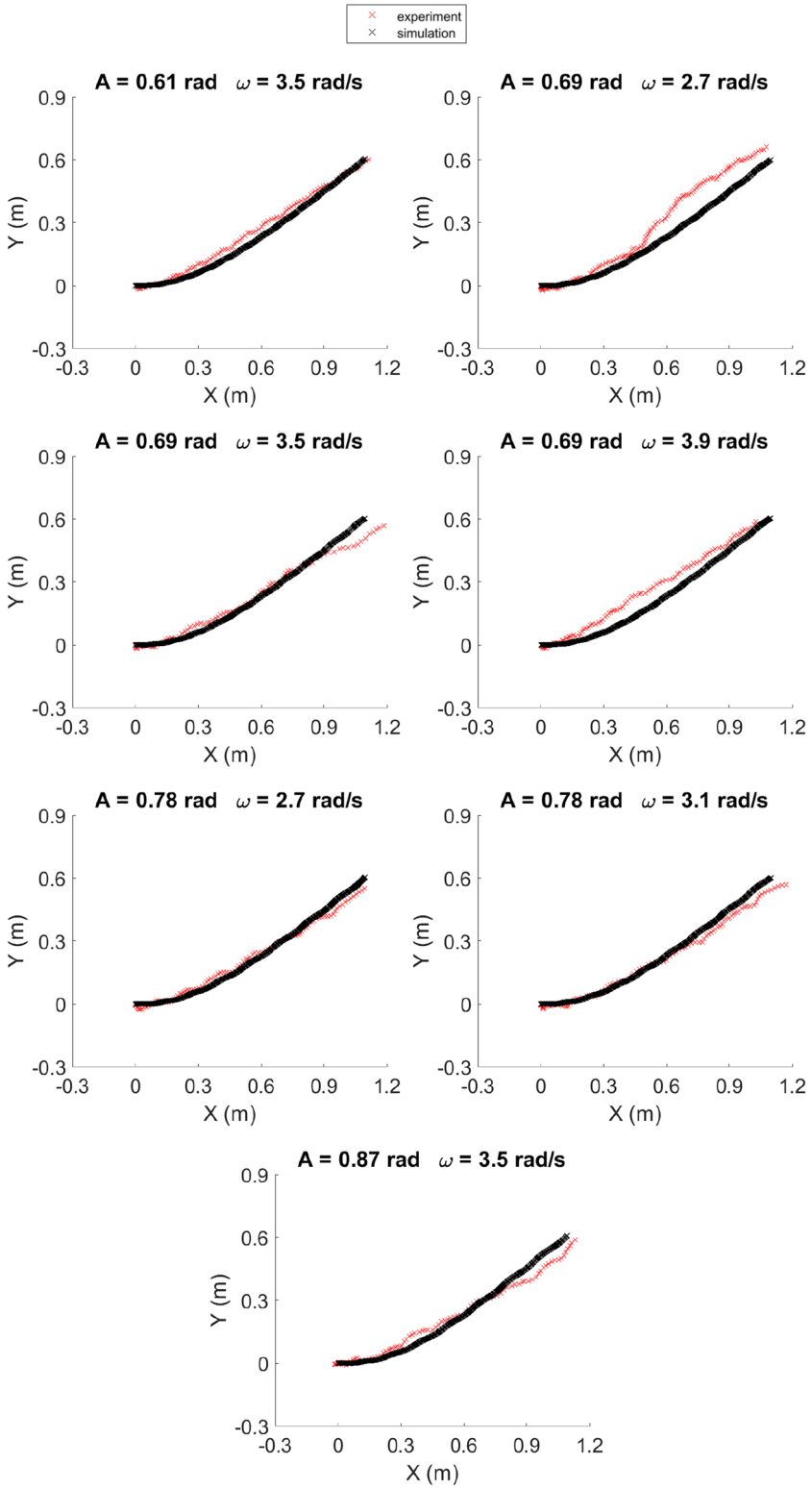

Fig. 13 Comparison of the positions of the robot along the trajectories obtained via experiments and simulations for turning motion

Appendix B: Index to Supplementary Materials

Supplementary materials	File type	Description
Multimedia Extension #1	Video	Comparison of the trajectories obtained from the experiment and the simulation for Path: 1
Multimedia Extension #2	Video	Comparison of the trajectories obtained obtained from the experiment and the simulation for Path: 2
Supplementary Data 1	.pdf	Estimation of low-level controller gains (k_p and k_d)
Supplementary Data 2	.xlsx	Fitness versus generation for straight motion
Supplementary Data 3	.xlsx	Fitness versus generation for turning motion

References

1. Kelasidi, E., Liljeback, P., Pettersen, K.Y., Gravdahl, J.T.: Innovation in underwater robots: Biologically inspired swimming snake robots. IEEE Robot. Autom. Mag. **23**(1), 44–62 (2016). https://doi.org/10.1109/MRA.2015.2506121
2. Raj, A., Thakur, A.: Dynamically feasible trajectory planning for anguilliform-inspired robots in the presence of steady ambient flow. Robot. Auton. Syst. **118**, 144–158 (2019)
3. Hollinger, G.A., Pereira, A.A., Binney, J., Somers, T., Sukhatme, G.S.: Learning uncertainty in ocean current predictions for safe and reliable navigation of underwater vehicles. J. Field Robot. **33**(1), 47–66 (2015). https://doi.org/10.1002/rob.21613
4. Hoy, M., Matveev, A.S., Savkin, A.V.: Algorithms for collision-free navigation of mobile robots in complex cluttered environments: a survey. Robotica **33**(3), 463–497 (2015)
5. Pereira, A.A., Binney, J., Hollinger, G.A., Sukhatme, G.S.: Risk-aware path planning for autonomous underwater vehicles using predictive ocean models. J. Field Robot. **30**(5), 741–762 (2013). https://doi.org/10.1002/rob.21472
6. Jardine, P.T., Givigi, S.: A predictive motion planner for guidance of autonomous UAV systems. In: 2016 Annual IEEE Systems Conference (SysCon), pp. 1–6. https://doi.org/10.1109/SYSCON.2016.7490514 (2016)
7. Hegde, R., Panagou, D.: Multi-agent motion planning and coordination in polygonal environments using vector fields and model predictive control. In: 2016 European Control Conference (ECC), pp. 1856–1861. https://doi.org/10.1109/ECC.2016.7810561 (2016)
8. Howard, T., Pivtoraiko, M., Knepper, R.A., Kelly, A.: Model-predictive motion planning: Several key developments for autonomous mobile robots. IEEE Robot. Autom. Mag. **21**(1), 64–73 (2014). https://doi.org/10.1109/MRA.2013.2294914
9. Kelasidi, E., Pettersen, K.Y., Gravdahl, J.T., Liljebäck, P.: Modeling of underwater snake robots. In: 2014 IEEE International Conference on Robotics and Automation (ICRA), pp. 4540–4547. https://doi.org/10.1109/ICRA.2014.6907522 (2014)
10. Suebsaiprom, P., Lin, C.L., Engkaninan, A.: Undulatory locomotion and effective propulsion for fish-inspired robot. Control Eng. Pract. **58**, 66 – 77 (2017). https://doi.org/10.1016/j.conengprac.2016.09, http://www.sciencedirect.com/science/article/pii/S096706611630199X
11. Scaradozzi, D., Palmieri, G., Costa, D., Pinelli, A.: BCF swimming locomotion for autonomous underwater robots: a review and a novel solution to improve control and efficiency, vol. 130. https://doi.org/10.1016/j.oceaneng.2016.11.055, http://www.sciencedirect.com/science/article/pii/S0029801816305613 (2017)
12. Verma, S., Xu, J.X.: Data-assisted modeling and speed control of a robotic fish. IEEE Trans. Ind. Electron. **64**(5), 4150–4157 (2017). https://doi.org/10.1109/TIE.2016.2613500
13. Ozmen Koca, G., Bal, C., Korkmaz, D., Bingol, M.C., Ay, M., Akpolat, Z.H., Yetkin, S.: Three-dimensional modeling of a robotic fish based on real carp locomotion. Applied Sciences **8**(2), 180 (2018)
14. Gus'kova, N., Makhortykh, G.V., Shcheglova, M.G.: Inertia and drag of elliptic cylinders oscillating in a fluid. Fluid Dyn. **33**(1), 91–95 (1998). https://doi.org/10.1007/BF02698165
15. Paidoussis, M.P.: 8 solitary cylindrical structures in axial flow. In: Slender Structures and Axial Flow, Fluid-Structure Interactions, vol. 2, pp. 787–1032. Academic Press. https://doi.org/10.1016/S1874-5652(04)80004-8, http://www.sciencedirect.com/science/article/pii/S1874565204800048 (2003)
16. Kelasidi, E., Pettersen, K.Y., Gravdahl, J.T.: A waypoint guidance strategy for underwater snake robots. In: 2014 22nd Mediterranean Conference of Control and Automation (MED), pp. 1512–1519, IEEE (2014)
17. Raj, A., Thakur, A.: Fish-inspired robots: design, sensing, actuation, and autonomy—a review of research. Bioinspir. Biom. **11**(3), 031001 (2016)
18. Epps, B., y Alvarado, P., Youcef-Toumi, K., Techet, A.: Swimming performance of a biomimetic compliant fish-like robot. Exper. Fluids **47**(6), 927–939 (2009). https://doi.org/10.1007/s00348-009-0684-8
19. Guan, Z., Gu, N., Gao, W., Nahavandi, S.: 3D hydrodynamic analysis of a biomimetic robot fish. In: 2010 11th International Conference on Control Automation Robotics & Vision, pp. 793–798. https://doi.org/10.1109/ICARCV.2010.5707359 (2010)
20. Lighthill, M.J.: Note on the swimming of slender fish. J. Fluid Mech. **9**(2), 305–317 (1960). https://doi.org/10.1017/S0022112060001110
21. Lighthill, M.: Aquatic animal propulsion of high hydromechanical efficiency. J. Fluid Mech. **44**(02), 265–301 (1970)
22. Lighthill, M.: Large-amplitude elongated-body theory of fish locomotion. Proc. R. Soc. Lond. Ser. B Biol. Sci. **179**(1055), 125–138 (1971)
23. Morison, J., Johnson, J., Schaaf, S.: The force exerted by surface waves on piles. J. Petrol. Technol. **2**(05), 149–154 (1950). https://doi.org/10.2118/950149-G
24. Boyer, F., Porez, M., Leroyer, A., Visonneau, M.: Fast dynamics of an eel-like robot - comparisons with navier stokes simulations. IEEE Trans. Robot. **24**(6), 1274–1288 (2008). https://doi.org/10.1109/TRO.2008.2006249
25. Boyer, F., Porez, M., Leroyer, A.: Poincaré–cosserat equations for the lighthill three-dimensional large amplitude elongated body

theory: Application to robotics. J. Nonlinear Sci. **20**(1), 47–79 (2010)
26. Ramananarivo, S., Godoy-Diana, R., Thiria, B.: Passive elastic mechanism to mimic fish-muscle action in anguilliform swimming. J. R. Soc. Interface **10**(88) (2013). https://doi.org/10.1098/rsif.2013.0667
27. Porez, M., Boyer, F., Ijspeert, A., et al.: Improved lighthill fish swimming model for bio-inspired robots-modelling, computational aspects and experimental comparisons. Int. J. Robot. Res. **33**(10), 1322–1341 (2014)
28. Clark, A.J., Tan, X., McKinley, P.K.: Evolutionary multiobjective design of a flexible caudal fin for robotic fish. Bioinspir. Biom. **10**(6), 065006 (2015). http://stacks.iop.org/1748-3190/10/i=6/a=065006
29. Wang, W., Zhao, J., Xiong, W., Cao, F., Xie, G.: Underwater Electric Current Communication of Robotic Fish: Design and Experimental Results. In: 2015 IEEE International Conference on Robotics and Automation (ICRA), pp. 1166–1171. IEEE (2015)
30. Wang, J., McKinley, P.K., Tan, X.: Dynamic modeling of robotic fish with a flexible caudal fin. In: ASME 2012 5th Annual Dynamic Systems and Control Conference joint with the JSME 2012 11th Motion and Vibration Conference, American Society of Mechanical Engineers, pp. 203–212 (2012)
31. Khalil, W., Rongere, F.: Dynamic modeling of floating systems: Application to eel-like robot and rowing system. In: 2014 IEEE 13th International Workshop on Advanced Motion Control (AMC), pp. 21–30. IEEE (2014)
32. Apneseth, C.C., Day, A.H., Clelland, D.: Hydrodynamics of an oscillating articulated eel-like structure. Ocean Eng. **37**(13), 1221–1232 (2010). https://doi.org/10.1016/j.oceaneng.2010.06.001
33. Kelasidi, E., Pettersen, K.Y., Gravdahl, J.T., et al.: Modeling and Propulsion Methods of Underwater Snake Robots. In: 2017 IEEE Conference on Control Technology and Applications (CCTA), pp. 819–826. IEEE (2017)
34. Kopman, V., Laut, J., Acquaviva, F., Rizzo, A., Porfiri, M.: Dynamic modeling of a robotic fish propelled by a compliant tail. IEEE J. Ocean. Eng. **40**(1), 209–221 (2015). https://doi.org/10.1109/JOE.2013.2294891
35. McIsaac, K.A., Ostrowski, J.P.: Motion planning for anguilliform locomotion. IEEE Trans. Robot. Autom. **19**(4), 637–652 (2003). https://doi.org/10.1109/TRA.2003.814495
36. Zuo, Z., Wang, Z., Li, B., Ma, S.: Serpentine locomotion of a snake-like robot in water environment. In: 2008 IEEE International Conference on Robotics and Biomimetics, pp 25–30. https://doi.org/10.1109/ROBIO.2009.4912974 (2009)
37. Nguyen, P.L., Lee, B.R., Ahn, K.K.: Thrust and swimming speed analysis of fish robot with non-uniform flexible tail. J. Bion. Eng. **13**(1), 73–83 (2016). https://doi.org/10.1016/S1672-6529(14)60161-X, http://www.sciencedirect.com/science/article/pii/S167265291460161X
38. Kanso, E., Marsden, J.E., Rowley, C.W., Melli-Huber, J.B.: Locomotion of articulated bodies in a perfect fluid. J. Nonlinear Sci. **15**(4), 255–289 (2005). https://doi.org/10.1007/s00332-004-0650-9
39. Zhang, A., Ma, S., Li, B., Wang, M., Guo, X., Wang, Y.: Adaptive controller design for underwater snake robot with unmatched uncertainties. Sci. China Inf. Sci **59**(5), 052205 (2016). https://doi.org/10.1007/s11432-015-5421-8
40. Ranganathan, T., Singh, V., Thondiyath, A.: Estimation of hydrodynamic parameters for underwater systems using a simple off-line regression method: a case study. J. Mar. Sci. Technol **24**(3), 968–983 (2019)
41. Chen, Z., Shatara, S., Tan, X.: Modeling of biomimetic robotic fish propelled by an ionic polymer–metal composite caudal fin. IEEE/ASME Trans. Mechatron. **15**(3), 448–459 (2010). https://doi.org/10.1109/TMECH.2009.2027812
42. Chan, W.L., Kang, T.: Simultaneous determination of drag coefficient and added mass. IEEE J. Ocean. Eng. **36**(3), 422–430 (2011). https://doi.org/10.1109/JOE.2011.2151370
43. Raj, A., Kumar, A., Thakur, A.: Automated locomotion parameter tuning for an anguilliform-inspired robot. In: 2016 IEEE International Conference on Systems, Man, and Cybernetics (SMC), pp. 002564–002569. https://doi.org/10.1109/SMC.2016.7844625 (2016)
44. Phamduy, P., Vazquez, M.A., Kim, C., Mwaffo, V., Rizzo, A., Porfiri, M.: Design and characterization of a miniature free-swimming robotic fish based on multi-material 3D printing. Int. J. Intell. Robot. Appl. **1**(2), 209–223 (2017). https://doi.org/10.1007/s41315-017-0012-z
45. Nakayama, Y.: Introduction to fluid mechanics. Butterworth-Heinemann, Oxford (2018)
46. Tran, M.Q., Nguyen, H.D., Binns, J., Chai, S., Forrest, A.L., et al.: Least squares optimisation algorithm based system identification of an autonomous underwater vehicle. PROCEEDING of Publishing House for Science and Technology **1**(1), 1–12 (2016)
47. Allotta, B., Costanzi, R., Pugi, L., Ridolfi, A.: Identification of the main hydrodynamic parameters of typhoon auv from a reduced experimental dataset. Ocean Eng. **147**, 77–88 (2018)
48. Avila, J.P.J., Adamowski, J.C., Maruyama, N., Takase, F.K., Saito, M.: Modeling and identification of an open-frame underwater vehicle: The yaw motion dynamics. J. Intell. Robot. Syst. **66**(1-2), 37–56 (2012)
49. Avila, J.P., Donha, D.C., Adamowski, J.C.: Experimental model identification of open-frame underwater vehicles. Ocean Eng. **60**, 81–94 (2013). https://doi.org/10.1016/j.oceaneng.2012.10.007
50. Randeni, P.S.A.T., Forrest, A.L., Cossu, R., Leong, Z.Q., Ranmuthugala, D., Schmidt, V.: Parameter identification of a nonlinear model: replicating the motion response of an autonomous underwater vehicle for dynamic environments. Nonlinear Dyn. **91**(2), 1229–1247 (2018). https://doi.org/10.1007/s11071-017-3941-z
51. Xu, H., Soares, C.G.: Vector field path following for surface marine vessel and parameter identification based on LS-SVM. Ocean Eng. **113**, 151–161 (2016). https://doi.org/10.1016/j.oceaneng.2015.12.037, http://www.sciencedirect.com/science/article/pii/S0029801815007040
52. Xu, F., Zou, Z.J., Yin, J.C., Cao, J.: Identification modeling of underwater vehicles' nonlinear dynamics based on support vector machines. Ocean Eng. **67**, 68–76 (2013). https://doi.org/10.1016/j.oceaneng.2013.02.006, http://www.sciencedirect.com/science/article/pii/S0029801813000863
53. Zare, E.M., Bozorg, M., Ebrahimi, S.: Identification of an autonomous underwater vehicle dynamic using extended kalman filter with ARMA noise model. Int. J. Robot. **4**(6), 22–28 (2015)
54. Eng, Y.H., Teo, K.M., Chitre, M., Ng, K.M.: Online system identification of an autonomous underwater vehicle via in-field experiments. IEEE J. Ocean. Eng. **41**(1), 5–17 (2016). https://doi.org/10.1109/JOE.2015.2403576
55. SAT, R.P., Leong, Z.L., Ranmuthugala, D., Forrest, A., Duffy, J.: Numerical investigation of the hydrodynamic interaction between two underwater bodies in relative motion. Appl. Ocean Res. **51**, 14 – 24 (2015). https://doi.org/10.1016/j.apor.2015.02.006, http://www.sciencedirect.com/science/article/pii/S0141118715000279
56. Dash, A.K., Nagarajan, V., Sha, O.P.: Bifurcation analysis of a high-speed twin-propeller twin-rudder ship maneuvering model in roll-coupling motion. Nonlinear Dyn. **83**(4), 2035–2053 (2016). https://doi.org/10.1007/s11071-015-2463-9
57. Liang, X., Li, Y., Peng, Z., Zhang, J.: Nonlinear dynamics modeling and performance prediction for underactuated

AUV with fins. Nonlinear Dyn. **84**(1), 237–249 (2016). https://doi.org/10.1007/s11071-015-2442-1
58. Kelasidi, E., Pettersen, K.Y., Gravdahl, J.T., Liljebäck, P.: Modeling of underwater snake robots. In: 2014 IEEE International Conference on Robotics and Automation (ICRA), pp 4540–4547. https://doi.org/10.1109/ICRA.2014.6907522 (2014)
59. Mehta, R.S., Ward, A.B., Alfaro, M.E., Wainwright, P.C.: Elongation of the body in eels. Integr. Comp. Biol. **50**(6), 1091–1105 (2010)
60. Kihiu, J., Ikua, B., Muvengei, O.: Dynamic analysis of multi-body mechanical systems with imperfect kinematic joints: A literature survey and review (2017)
61. Chaudhary, H., Saha, S.K.: Dynamics and balancing of multibody systems, vol. 37. Springer Science & Business Media (2008)
62. Kelasidi, E., Pettersen, K.Y., Liljebäck, P., Gravdahl, J.T.: Integral line-of-sight for path following of underwater snake robots. In: 2014 IEEE Conference on Control Applications (CCA), pp. 1078–1085. https://doi.org/10.1109/CCA.2014.6981478 (2014)
63. Fossen, T.I.: Handbook of marine craft hydrodynamics and motion control. Wiley, New York (2011)
64. Mobayen, S., Baleanu, D., Tchier, F.: Second-order fast terminal sliding mode control design based on LMI for a class of non-linear uncertain systems and its application to chaotic systems. J. Vib. Control. **23**(18), 2912–2925 (2017). https://doi.org/10.1177/1077546315623887
65. Petráš, I.: A note on fractional-order non-linear controller: possible neural network approach to design. In: 2016 International Joint Conference on Neural Networks (IJCNN), pp. 603–608. https://doi.org/10.1109/IJCNN.2016.7727255 (2016)
66. Pan, Y., Kumar, K., Liu, G.: Extremum seeking control with second-order sliding mode. SIAM J. Control. Optim. **50**(6), 3292–3309 (2012). https://doi.org/10.1137/090778481
67. Švec, P., Thakur, A., Raboin, E., Shah, B., Gupta, S.: Target following with motion prediction for unmanned surface vehicle operating in cluttered environments. Auton. Robot. **36**(4), 383–405 (2014). https://doi.org/10.1007/s10514-013-9370-z
68. Cardoso, V., Oliveira, J., Teixeira, T., Badue, C., Mutz, F., Oliveira-Santos, T., Veronese, L., Souza, A.F.D.: A model-predictive motion planner for the iara autonomous car. In: 2017 IEEE International Conference on Robotics and Automation (ICRA), pp. 225–230. https://doi.org/10.1109/ICRA.2017.7989028 (2017)

Aditi Raj received a Ph.D. degree in mechanical engineering from the Indian Institute of Technology Patna in 2019 and Bachelor of Technology (B.Tech.) degree in mechanical engineering from the University College of Engineering and Technology, Hazaribag in 2013. Her research interests include design, control, and motion planning of bio-inspired robots. Her review paper titled 'Fish-inspired robots: design, sensing, actuation, and autonomy-review of research' was selected in Bioinspiration & Biomimetics journal's Highlights of 2016.

Atul Thakur is an Associate Professor in the Department of Mechanical Engineering at Indian Institute of Technology Patna. His research interest is broadly in the area of robotics and automation. He has been actively engaged in the research involving the design, motion planning, and control of bio-inspired robots, application of robotics in the area of solid waste management, and selective micromanipulation of biological cells using magnetic microrobots. He received a Ph.D. degree in mechanical engineering from the University of Maryland, College Park, Master of Technology (M.Tech.) degree in manufacturing engineering from the Indian Institute of Technology Bombay, and Bachelor of Engineering (B.E.) degree in production engineering from the University of Mumbai. Atul is a recipient of the 2013 Best Dissertation Award from ASME - CIE Division. He received Elsevier Journal of Computer-Aided Design 2012 most cited paper award. He is also a member of the American Society of Mechanical Engineers (ASME) since 2009 and Institute of Electrical and Electronics Engineers (IEEE) since 2011.